2010

Multi-pole permanent magnet motor design and control for high performance electromechanical actuation in all electric aircraft

Jared C. Bindl
University of Central Florida

MULTI-POLE PERMANENT MAGNET MOTOR DESIGN AND CONTROL FOR HIGH PERFORMANCE ELECTROMECHANICAL ACTUATION IN ALL ELECTRIC AIRCRAFT

by

JARED C. BINDL

A Thesis submitted in partial fulfillment of the requirements
for the Honors in the Major Program in Electrical Engineering
in the College of Electrical Engineering and Computer Science
and in the Burnett Honors College
at the University of Central Florida
Orlando, Florida

Summer Term
2010

Thesis Chair: Dr. Thomas Xinzhang Wu

ABSTRACT

The evolution of aircraft has led into a large increase in the demand for electrically integrated subsystems. Part of this demand is the transformation of a centralized hydraulic system to independently operated electrical subsystems. The result of this overhaul will decrease aircraft weight, increase reliability, reduce aircraft lifetime maintenance and cost, and help to increase the control of power distribution.

This thesis proposes the design methodology of a multi-pole permanent magnet (PM) motor with a capability to operate at high temperature. High temperature capability is one of the key requirements to implement electromechanical actuation for aircraft flight control, replace hydraulic actuation system, especially in tactical military aircraft, due to the hot environment and lack of heat sink. Temperature effects on motor materials are reviewed. The need for high power density is considered in the design. The motor design is confirmed by ANSYS RMXprt software. Along with the motor design, a voltage control method is also designed for the motor. Integrated electrical simulation results of the motor and controller to follow highly dynamic flight profiles are provided to show the stroke tracking, input power (including regenerative power), and winding copper loss. Experimentation set-up of EMA and experimental uncertainties are also discussed

ACKNOWLEDGMENTS

Throughout the process of this thesis I have been mentored, trained, enlightened, and educated by some truly extraordinary people. The hard work and effort put into this paper was not a single effort and I owe much appreciation to those who assisted me along the way. The experience and understanding I have attained from this endeavor has not only increased my appetite for knowledge, it has given me confidence in pursuing graduate level education.

I would first like to mention the admiration of my thesis advisor and committee chair, Dr. Thomas Xinzhang Wu, for his astounding work ethic, sound academic and research philosophy, as well as the setting of creativity that he creates for his students to thrive in. His mentorship and guidance has been invaluable and has made this process both challenging and rewarding.

My thanks extend to all my committee members Dr. Issa Batarseh, Dr. Louis Chow and Dr. Quinn Leland. Without their insight, comments, and constructive criticism the quality of this work would not be held to the highest standards. A special thanks is allotted to Dr. Leland for her support and accommodation at AFRL in Dayton, OH and the experience I gained from my summer visit. This work is supported by the U.S. Air Force under Contract: FA8650-09-2-2940 and UCF Undergraduate Research Fellowship.

I would also like to take this opportunity to thank my fellow lab mates, Dr. Wendell Brokaw, David Woodburn, Yang Hu, Hanzhou Liu, and Kejiu Zhang for their

ability to provide insight to the research experience from the graduate level as well as offer new friendships. In addition I would like to mention my deep appreciation for the personal mentorship, articulate teaching, and unrelenting dedication of David Woodburn. His example has given me new found inspiration to follow in the research process, and I am forever grateful for this.

Finally, I would like to thank the family that has always been there to support me along the way. They have provided the encouragement, inspiration, and advice when I needed it most. Specifically, thanks to my aunt, Debi Bindl, mother, Tammy Kleinvachter, step mother, Melissa Bindl, father, Edward Bindl, sister, Leyna Bindl, grandmothers, Donna Bindl and Connie Gaskill, and last but not least my Grandfather Mike Gaskill.

TABLE OF CONTENTS

LIST OF FIGURES

LIST OF TABLES

CHAPTER ONE: INTRODUCTION

1.1 All Electric Aircraft

The progress and development toward all electric aircraft have been a vision of the aerospace industry for decades. The idea is far from a new idea but the trend has been a slow yet steady process and shows much promise for tomorrow's aircraft in a variety of ways. When considering the term "all electric," this is referring to all onboard systems to be powered by electricity excluding jet propulsion [1]. The pace of transformation of aircraft to more electric integration is largely due to the increase in aircraft system loads [2]. Currently a large proportion of today's civilian and military aircraft are occupied by integrated electrical subsystems giving headway toward the all electric aircraft. However, there is still one major overhaul to be included in the mix of integrated electrical subsystems.

The actuation system of most modern aircraft has been left to hydraulic systems. This is largely due to the fact that hydraulics produces a large amount of force in the actuation of control surfaces [3]. There are three types of actuation: flight control; utility; and propulsion. For flight control, there are two categories, primary flight control and secondary flight control. Utility actuation includes landing gears, bay doors, etc. There are advantages to maintain hydraulic systems; however, the long term effects of electromechanical actuators (EMAs) in the aviation industry outweigh these advantages. A reduction in maintenance, decreased overall weight thus lower fuel consumption, lower

purchasing and operating cost, and higher flexibility of power control are a few of the desired effects of electromechanical actuation [3].

Increased efficiency in electrical power generation and load management modes of modern aircraft has led to power savings. Integrating primary and secondary control surfaces to the load management of the system could create further power savings and make troubleshooting of the actuation system more manageable [3]. The transformation of a centralized hydraulic system to independently operated electrical subsystems is ultimately the goal. As with many major overhauls there are challenges along the process.

There are two prevalent concerns with this implementation [4]. The first concern is the challenge of providing an appropriate thermal management system to effectively remove heat from this newly integrated system. The other concern from EMA research and development has been a tendency for jamming. Fault tolerance techniques, also known as health prognostics, is a field of research aimed at preventing actuator jamming. Considering that proper operation of primary flight control is paramount, it is obvious that limited tolerance is critical to EMA development. Heat generation in an EMA system is transient and highly localized resulting from the removal of hydraulic fluid [5]. These localized heat areas are more of a concern in the primary controls where there is constant actuation provided to these surfaces and only a limited heat sink. The localized heat generation in the secondary controls are less of a concern due to the time interval between activation. There is enough time allowed for proper heat dissipation in the case of secondary flight controls [5]. When considering higher performance aircraft temperature spikes become more concerning. For a highly robust military fighter jet at

supersonic speeds rapid acceleration or sharp maneuvering creates higher demand for an innovative thermal management system. Coupling of all electrical subsystems can and will make heat more mitigated along with more efficient power distribution.

1.2 Electromechanical Actuation

As mentioned above, electromechanical actuation is being looked as a more reliable long term source for primary flight control operation for a number of reasons. The challenges that must be overcome, however, are very significant. A brief background on actuation will help to paint the picture for overall benefits of the EMA. Hydraulic actuators have been the conventional method for actuation for many decades and as a result the system integration and implementation are solid [1]. High reliability becomes a huge benefit to this method.

The problem with hydraulic actuation is weight and maintenance. Weight accumulation by the actuators themselves and the hydraulic fluid are a big consideration in overall aircraft design. Leaks can often spring in a hydraulic system making the maintenance of the system very tedious [1]. The following figure shows an example of the conventional hydraulic actuator and its components.

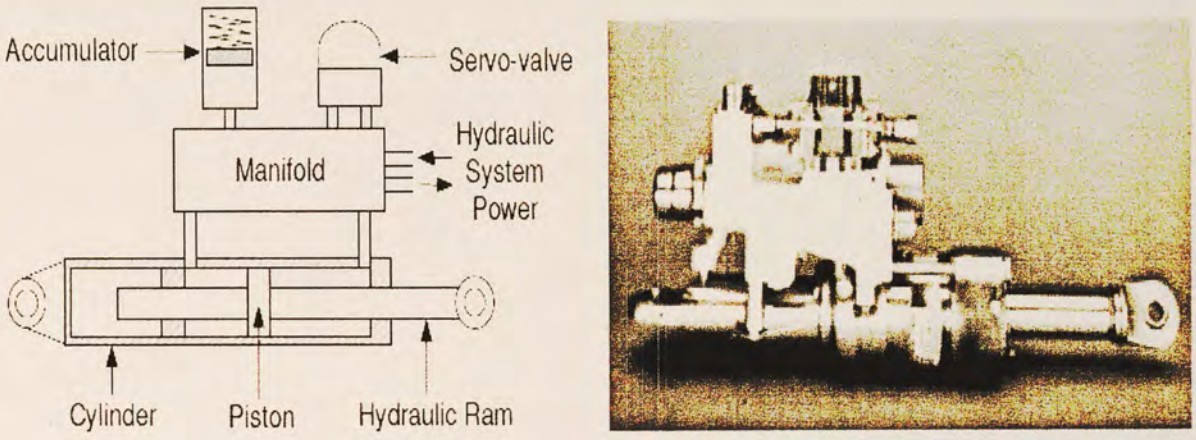

(a) Typical FBW Actuator Components (b) FBW Hydraulic Actuator

Figure 1-1: Conventional Hydraulic Actuator [1]

Another alternative to actuation is the electro-hydrostatic actuator (EHA). This particular kind of actuation is a hybrid of a localized hydraulics and electric pump [1, 3]. By removing the hydraulic reservoir as well as the lines and fittings, which are the most problematic, and having a localized circuit at each actuator the system no longer has to be continually pressurized. Smaller reservoirs are assigned to actuator areas and operate with "pressure on demand" [1]. As with the EMA, the EHA still has localized heat problems creating higher operating temperatures and thus decreasing reliability.

While this type of actuation seems like a happy medium between hydraulic actuation and electromechanical actuation, the weight of the actuator itself is twice as heavy as a hydraulic actuator. The EHA still offers an overall weight, cost, and energy saving through "on-demand" operation. As will hydraulic actuators EHAs are still prone to leaks so maintaining them is still a considerable issue as well. The EMA now has progressed to become the best overall replacement of the hydraulic actuator for its long term benefits.

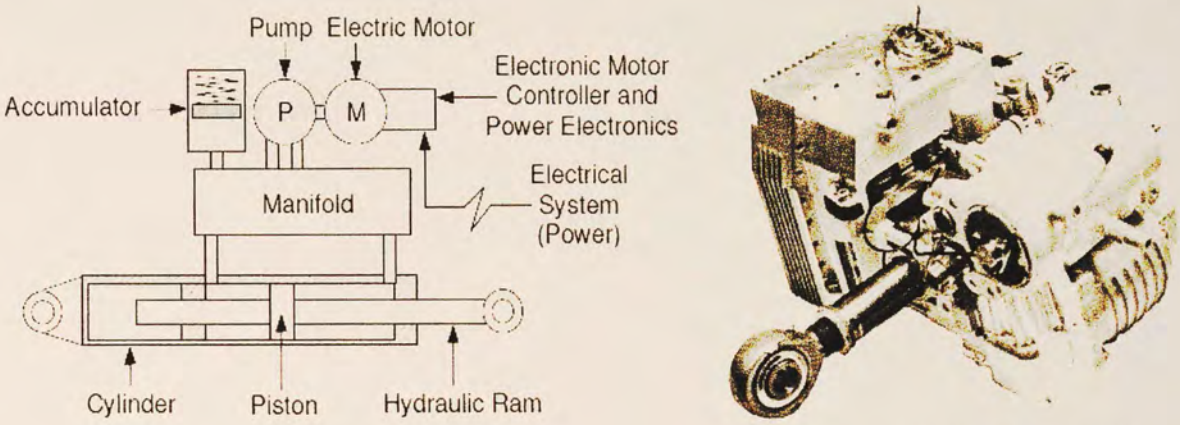

(a) Typical EHA Components

(b) Prototype Flight Control EHA

Figure 1-2: Electro-Hydrostatic Actuator (Photo from [1])

Generally an EMA consists of a ball and screw linear actuation system, power electronics, and a mechanical transmission. There are different types of actuation but for the purposes of this thesis and use of the EMA for flight controls, a linear actuation system is the only type described here. The actuator seen in Figure 1-3 is an actual actuator used in an aircraft that serves multiple purposes. These functions include the actuation of flight surfaces, landing gear deployment and retraction, steering of antennas, and opening of cargo doors.

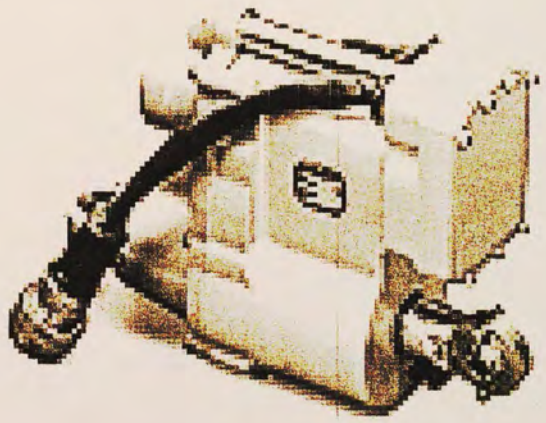

Figure 1-3: EMA Used in Aircraft

Again the major advantages of the EMA is its lack of hydraulic fluid, reducing maintenance, better energy efficiencies, and more efficient actuation movement. With no hydraulic fluid there is no chance of having leaks and thus less hazard of fire. The installation of hydraulic systems and replacements of pumps is not a quick task in aircraft maintenance. With EMA implementation the installation of electric motors and EMAs will be much easier. The "power on" demand feature helps with energy efficiencies of the aircraft [1]. This simply means that when the EMA is supplied with power when needed.

The movement and action of the EMA are also more responsive and sharp due to electro-mechanical control. This results in more accurate and efficient movement. In hydraulic action, fluid must be supplied by pumps therefore resulting in losses due to this action. The appeal of the EMA according to Air Force INVENT program is its energy efficiency and therefore thermal management. The implementation challenges as described earlier are becoming less and less of a concern through both industry and government sponsored research and development, further proving EMA technology to be a good solution to primary flight controls. Past utilization of EMAs were only used for less demanding flight control systems such as aircraft trim.

When addressing the concerns of EMA implementation in an aircraft these effects are only magnified with high performance aircraft. Providing a solution for these aircraft will solve the EMA issue for a variety of other aircrafts. Removing localized heat from the EMA, decreasing the size and weight of the system, and ensuring jamming tolerance

of the EMA in high performance aircraft will open the doors for large transformations in industry.

1.3 EMA Thermal Management

Lack of hydraulic fluid as coolant in the electric actuation system as described, and localized heat due to the electronics of the EMA have raised the issue of whether a unique thermal management system is necessary for the EMA overhaul. In a conventional hydraulic flight control actuation system the heat dissipation was accomplished through the circulation of the hydraulic fluid. For the EMA, there is no fluid as an effective heat sink, therefore, its thermal management has become a greater concern [5].

Inefficiencies in a system are the cause for heat generation. In the EMA system the main components are the electric motor, motor drive, and the gearbox. There are also two states to consider in terms of efficiencies: steady state; and transient states. For steady conditions the general efficiencies are 93% for the motor drive, 80% for the motor, and 80% for the gearbox [5]. For example, in the electric motor the resistivity of copper windings increases as the temperature increases causing inefficiencies. Losses due to magnetic materials due to temperature increase have the same effect. These losses will be later described in further detail.

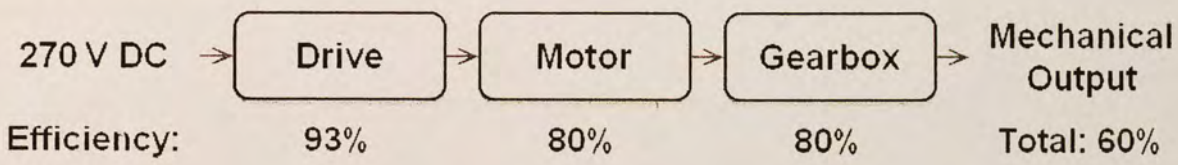

Figure 1-4: Block Diagram of Steady-state Efficiencies [5]

When considering a strike fighter aircraft transients become a major factor. This translates to higher amounts of losses in the different components of the EMA system. Traditional methods of heat removal to heat sink include aircraft fuel, bleed air, and through heat exchangers in hydraulic fluid. In a hydraulic system thermal transport of the fluid is accomplished through piping and reservoirs [1]. When the fluid is transferred to the reservoir it is run through heat exchangers and uses the fuel tanks as a heat sink. The convection to ambient air as the fluid travels through the pipes acts a heat sink while thermal transport is performed as well [1].

Therefore, in helping to resolve the thermal challenge for the EMA methods of heat sinks, thermal transport, and transient heat storage are needed. Choices of proper heat sinks are imperative. As with any design there are generally tradeoffs for cost, efficiency and performance. While fuel is considered a great heat sink and is used for cooling many components on an aircraft as fuel steadily decreases, the temperature increases as a result. Typical solutions for heat sinks considered for EMA application will generally include fuel tanks, cabin bleed air, or air from windblown wing surfaces [1, 5].

The transport of heat from the EMA could be accomplished through designs like loop heat pipes, loop thermosyphon, RAM air, or a few others. As an example, loop heat pipe transports heat passively from heat source to heat sink through phase change and capillary forces. The concept is that a cold plate will be placed near the source of heat, where inside the pipe which is attached to the plate is an evaporating liquid [6]. As heat

is transferred to the pipe the liquid evaporates and is sent to the heat sink where it can condense and return back to the heat source through another pipe [6]. This method is very desirable due to its passiveness, long distance transport, and ability to function in high g force environments.

Finally the third component to the thermal solution is heat storage. Erratic temperature spikes in a system may be a result of very demanding maneuvers or other transients. Generally a system is designed to accommodate maximum limit values. In this case however, a transient heat spike occurs at a very short time period, and to design the system for this circumstance may mean much more complicated and costly solution. When the average heat output is significantly lower than peak heat output a heat storage method is a good solution [7]. Heat storage techniques can help to solve this issue without a more demanding design in the thermal transport and heat sink area.

1.4 Permanent Magnet Motor

The type of electric motor that is generally used in an EMA design is the permanent magnet (PM) motor. When comparing PM motor rotors versus rotors that require electromagnetic excitation, the benefit is evident in aircraft EMA implementation. Permanent magnets do not require an excitation because they are already permanently magnetized. This eliminates copper loss on the rotor. Reliability at high speeds contributes to the strengths of the PM motor as well. Another major benefit of this type of motor is its simplicity maintenance friendly capability [8].

In PM motors the rotor contains permanent magnets while the stator contains electrical windings through slotted sections. The rotor and stator core consists of a few different components. Stripping away the stator coils and voltage circuitry, the stator core consists of stator slots that house the coils. The stator core is usually made of an iron composite containing favorable magnetic properties. There are various types of slot designs as well. Details of the design will be explained in Chapter 2.

Stator windings are simply copper wires that wrap around the stator slots in different configurations. Current passing through these windings induces the alternating magnetic field. The winding configuration, or method of wrapping the wire in the stator slots, is another critical design efficiency consideration. The rotor contains the rotor shaft and permanent magnets. The current in the stator windings applying the alternating magnetic field, combined with the alternating poles of the permanent magnet, cause the rotation in the motor.

The amount of space that the EMA system consumes is obviously a concern in overall design. Thus greater volumetric occupation by this adapted subsystem is reduced by the high power density PM motor [3]. PM motors have a high power density but is limited to the strength of the permanent magnet. Based on this reduction in volumetric occupation the localized thermal management solution for specified operation is created. Specifications of the operation of the motor may be increased to reduce overall volume; however, efficiency of the motor is thus compromised.

The design used in simulation for this thesis is a general design but is intended to integrate the permanent magnet design for high energy density, very robust and adaptive control schemes, and wire capable of withstanding high temperatures as well as very

dynamic temperature ranges. This development will contribute to the ability of the motor to operate in harsh environmental conditions. Material selection in a motor have a lot to do with the temperature ranges that a motor can withstand. The permanent magnet selection relates directly to dynamic and high operating temperature ranges of the motor.

1.5 Temperature Effects on Motor Materials

Heat generation in a system is always a concern for performance. When dealing with magnetic materials or materials in general a concern of degradation of the properties of the material are always kept in mind. When analyzing the operating temperature of a system, the peak value of that temperature is the value at which the specifications must be met. Stator windings are made of copper therefore the temperature effects in relation to the resistivity of these windings is necessary to evaluate. As temperature increases, resistivity increases. Normally, electrons try to move from one end of a wire to the other end under the influence of the applied electric field. As the temperature increases, the atomic vibrations increase, knocking the electrons off course in random directions. This reduces the flow of electrons or, more macroscopically, of current. The result is increasing resistance in the copper wire. This will increase the winding copper loss of the motor when temperature increases. Figure 1-5 shows that the copper resistivity is a linear function of temperature:

$$\rho(\mathrm{n}\Omega \cdot \mathrm{m}) = 15.4\left[1 + 0.0045\,1(T - 273)\right] \tag{1.1}$$

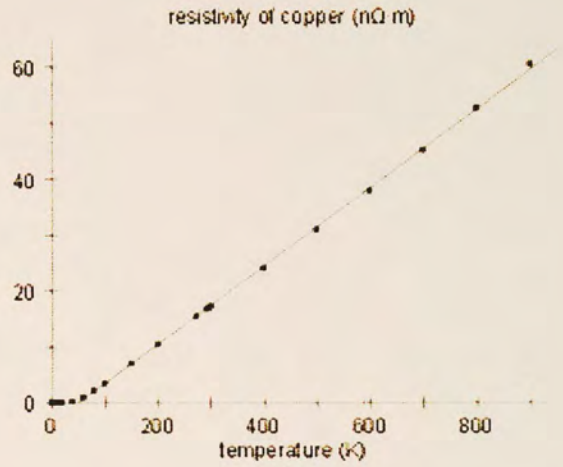

Figure 1-5: Temperature Dependence of Resistivity of Copper [6]

Stator core materials are made of soft magnetic materials. For this design the goal is to reduce size as well as increase operation temperature. In practical motor, Hiperco50 material may not be used due to cost, but it will be examined here. Unlike other soft magnetic materials that saturate at magnetic flux density of 1.5 Tesla, Hiperco50 saturates at 2.3 Tesla [9]. This translates in the ability to reduce rotor volume, and reduce iron core loss, thus increasing efficiency and power density. The operating temperature can be as high as 350°C.

The magnetic permeability, μ, of soft magnetic materials to be used for stator iron can be strongly affected by temperature. An analysis of sendust alloy [10] shows (Fig. 1-6) this dependence for two of its variants (D: 84.68% Fe, 9.15% Si, 6.17% Al; and G: 84.97% Fe, 9.47% Si, 5.56% Al, where the percentages are by weight).

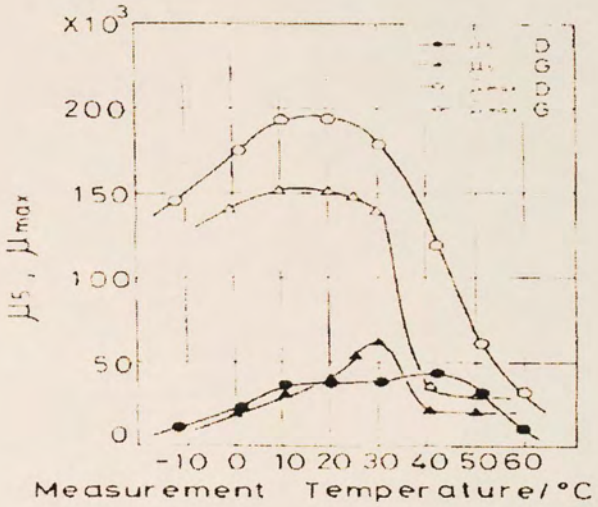

Figure 1-6: Temperature Dependence of Initial, μ_S, and Maximum, μ_{max}, Permeability of Two Variants of Sendust Alloy [10]

Here, we see that the magnetic permeability of this soft magnetic material drops when temperature is increased to 60° C to just a fraction of its highest value near room temperature. Permeability is the ratio of magnetic flux density, *B*, to magnetic flux intensity, *H*. Because magnetic permeability is not constant over the range of *H*, two key values of permeability are chosen: μ_S, the initial permeability at *H* = 5 mOe (0.4 A/m), and μ_{max}, the maximum permeability as seen in Figure 1-7.

When permeability of soft magnetic material drops, more current is required to keep the same torque of the motor. This will increase the power loss of windings.

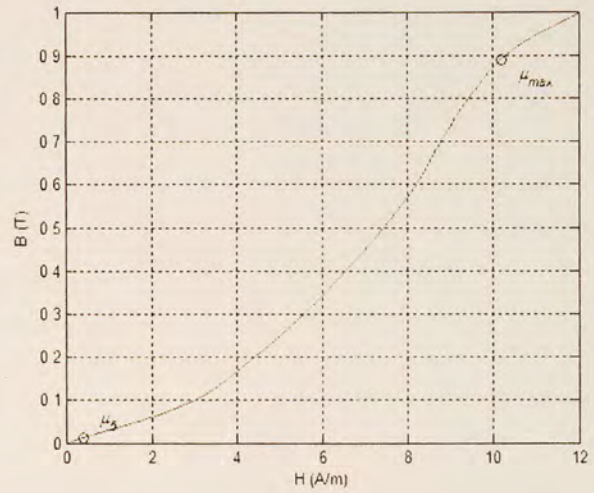

Figure 1-7: Initial and Maximum Permeability on a Typical BH Curve [11]

What permanent magnet is used in a design on rotor is based on application, cost, and specifications. PM motors today need high operating temperatures in order to maintain proper efficiency in high performance situations. The two permanent magnets, NdFeB and SmCo, are two of the most popular permanent magnets used today. Below we briefly examine the temperature effects of these two magnets. However, before these relationships can be understood a little background of the magnet hysteresis loop and terminology (Figure 1-8) must be given.

The magnetic material selection is based strictly on the temperature requirement. Samarium Cobalt (SmCo) can operate at 350°C. However there are two different series of this magnet. The first series is 1:5 and the second is 2:17. SmCo 2:17 is the magnet that will provide the proper response to 350°C. Although SmCo is the second strongest magnet next to Neodymium Iron Boron (NdFeB), NdFeB is unable to meet the max temperature requirements of our design. The strongest magnet on earth is Neodymium Iron Boron (NdFeB). However, the suggested operating temperature for NdFeB is only

150°C thus weakening the magnetic strength at temperatures up 150°C. SmCo have Maximum Energy Products that range from 16 to 32 Mega-Gauss Oersteds, and their theoretical limit is 34 MGOe [12]. The suggested operating temperature is the temperature above which the magnet's strength will be weakened.

Electromagnetic field comparison to the induced field in the magnet is seen in Fig. 1-8 as represented by the curve. The magnitude of the applied field also called the 'H' axis is represented in the horizontal axis. Induced field is represented by the vertical axis or 'B' axis [13]. If we sum the applied field and the contributions of the field of the magnet you will see the representation below as the normal or green curve. If we want only the field represented by the magnet we subtract the H field from the B curve to give us the blue intrinsic curve. This curve is called the "B-H" or intrinsic curve [13].

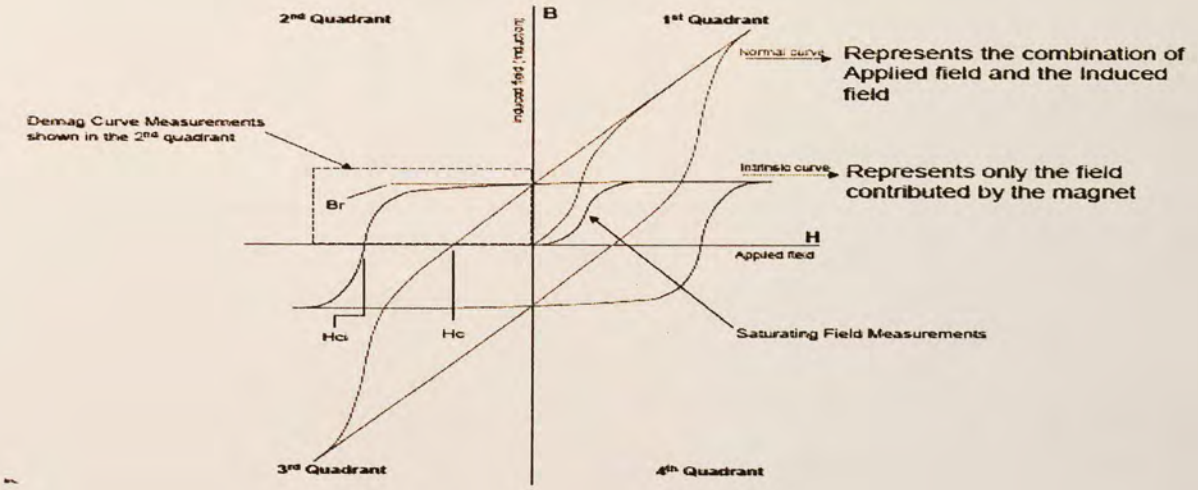

Figure 1-8: The Hysteresis Loop and Magnet Terminology [13]

Notation in Figure 1-9 is key to understanding temperature effects. Magnetic strength of the magnet or B_r (remanence or remnant induction) is seen on the vertical

axis. The value H_{ci} represents the magnet's resistance to demagnetization. The shape of the intrinsic curve can be constructed by H_k. To get H_k a horizontal line at the level of $0.9B_r$ is made. Where this line intersects the intrinsic curve, a vertical is dropped to the H axis creating the H_k point. H_k/H_{ci} is a measure of loop squareness [13]. Initial and maximum permeability of M-5 grain oriented steel at DC field. How the magnet reacts to demagnetizing stress determines the whether it is has good or poor loop squareness. A magnet with poor loop squareness will breakdown under high temperatures for example and lose magnetization. Performance at elevated temperatures can be indicated by both H_k and H_{ci} to ensure satisfactory magnet [13, 14].

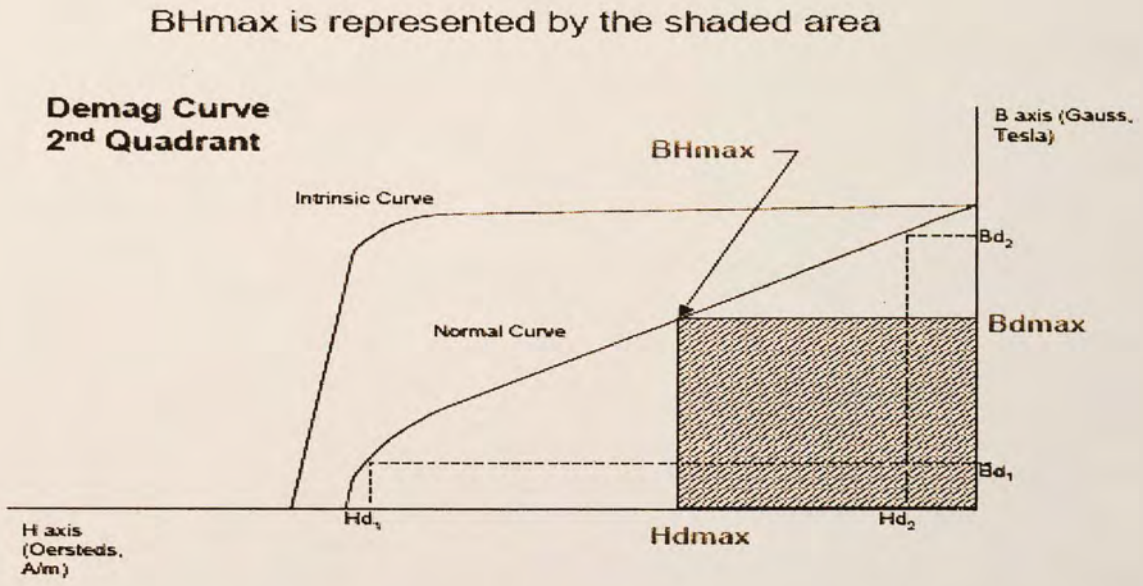

Figure 1-9: Maximum Energy Product (BH_{max}) [14]

Looking at temperature effects specifically, we will consider the second quadrant of the PM motor hysteresis loop. As seen in the Figure 1-10 for NdFeB it seen that both H_c (Magnetic Coercivity) and B_r (Magnetic Remanance) are reduced significantly as the

temperature ranges from 20 °C to 150 °C. H_c is reduced the most rapidly decreasing from 24 kOe to 8 kOe. This simply means that the magnet becomes weak at high temperatures and thus large performance losses in the motor.

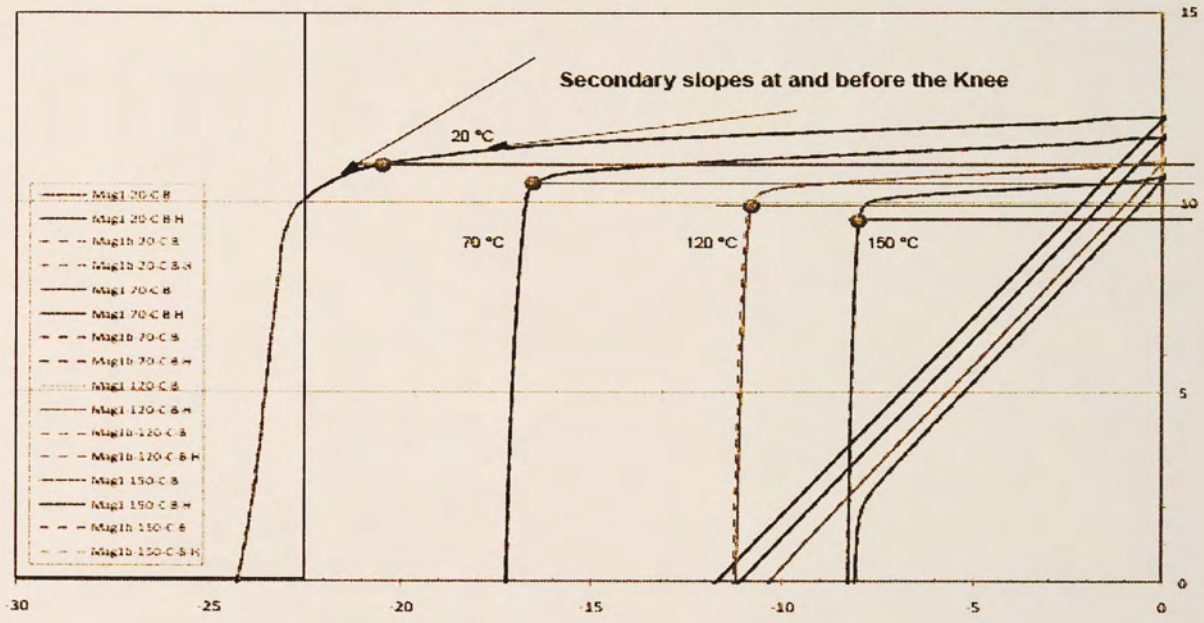

Figure 1-10: Temperature Effects on NdFeB [14]

If we analyze the temperature graph below the same as the NdFeB graph (Fig. 1-11) it is seen that despite the fact that SmCo does not have as high a value of magnetic coercively at room temperature, it does not decrease as fast at higher temperatures.

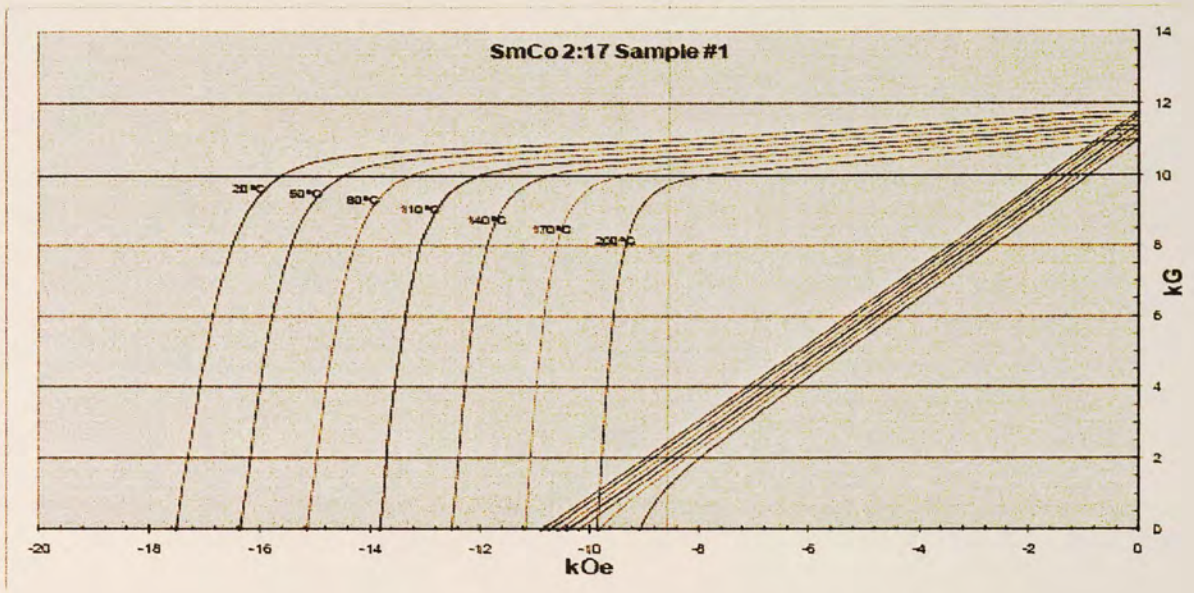

Figure 1-11: Temperature Effects on SmCo [14]

The following Figure 1-12 shows a good representation of the temperature effects of both the magnets in one graph. The tan lines are NdFeB and the blue lines show SmCo. Starting from 20 °C NdFeB shows to have a higher H_c and B_r value representing are stronger magnet at room temperature. NdFeB has an H_c value of approximately 30 kOe and a B_r value of 11 kG. SmCo has an H_c value of approximately 19 kOe and a B_r value of 10.8 kG. However, if we look at the values at 220 °C The H_c of NdFeB drops at a much greater rate than SmCo. Here NdFeB has an H_c value of approximately 4 kOe and a B_r value of 8.8 KG. SmCo has an H_c value of approximately 10 kOe and a B_r value of 10 kG. This diagram (Fig. 1-12) clearly shows that SmCo operates better at high temperatures as well as a wider variety of temperatures but is not quite as strong under cooler conditions [15].

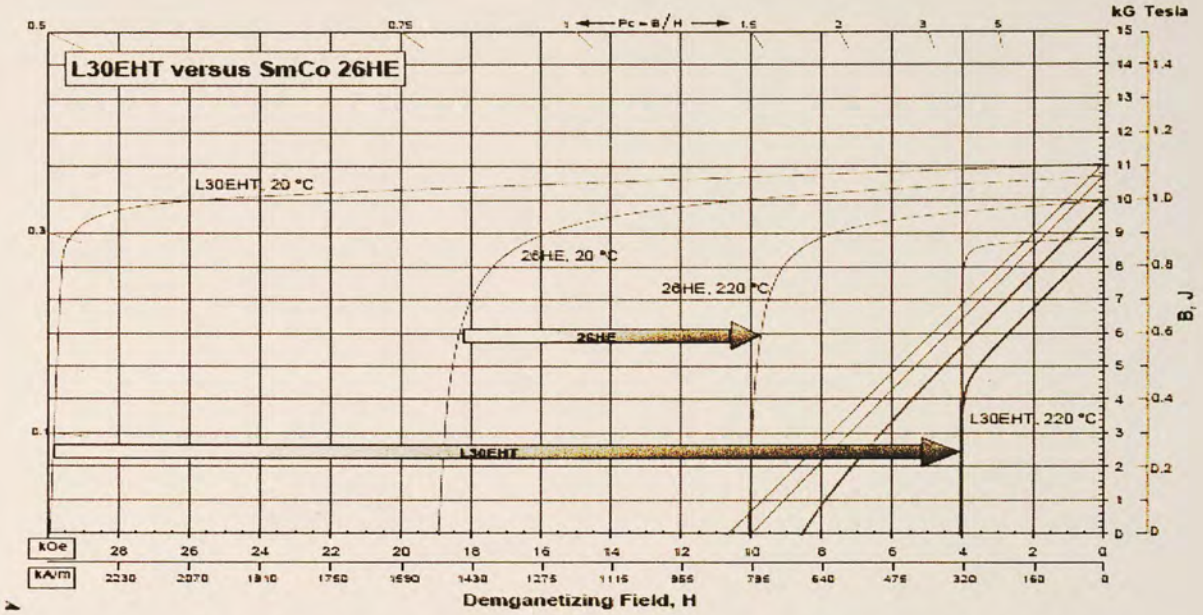

Figure 1-12: Comparison of Temperature Effects on NdFeB and SmCo [14]

Stator windings generally have operating temperature of 180-200°C maximum with common insulation. Fiberglass is a material made up of tiny glass fibers with very high heat tolerance. Using a fiberglass as the insulation in a double wrap technique creates an operating temperature of up to 450°C. This makes fiberglass an ideal choice for the design.

Insulating materials deteriorate and fail primarily due to high temperatures. The high temperatures of motors cause thermal stress on the insulation. Therefore, winding insulation must be thermally tested. Primarily, the rate of thermal degradation, an oxidation process, is governed by the Arrhenius rate law. The life of the insulation (L, in hours) is related to the temperature (T, in K) by

$$L = Ae^{\frac{B}{T}} \tag{1.2}$$

where A and B are considered constants. Based on this, it is fairly accurate to say that the insulation life decreases by 50% for every 10 °C rise in temperature. This equation is used in accelerated aging tests and for defining the insulation thermal classes (Fig. 1-13) (e.g. A,B,F, and H).

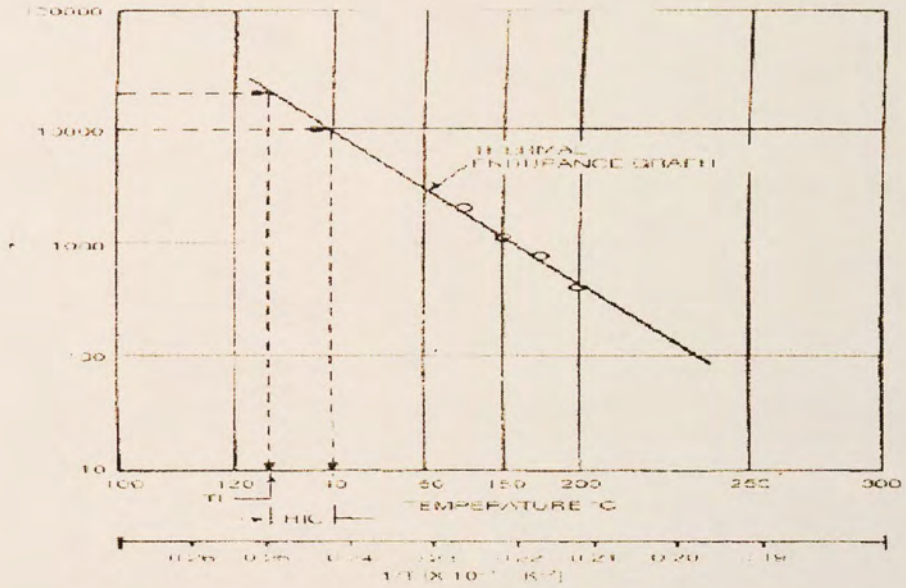

Figure 1-13: Typical Class B (Class 130) Thermal Endurance [16]

1.6 Inefficiencies and Losses

Understanding the losses in a PM motor is critical to understanding motor characteristics and design techniques. When considering losses this is directly related to power loss in the motor and thus temperature rise. There are four categories of losses in the PM motor: stator losses; rotor eddy current loss; windage loss, and bearing loss [17]. Each of these categories can be broken down into more specific loss effects, which will

be described to help understand design methodology.

When considering losses in the stator the materials that are associated with this are the stator core materials and the copper windings that wrap around its slots. The other side of Stator loss is the copper loss. Copper loss can be broken into two subcategories. Typical current losses from a conducting wire are I^2R losses and stray losses [17]. The resistance of a conducting wire creates this loss. When currents are passed through conducting wire naturally heat will be generated.

$$P_{Cu} = m_1 I^2 R \tag{1.3}$$

where m_1 represents the number of phases, 'I' represents current, and 'R' resistance. Stray losses in the copper windings are best described with electrical phenomenon called skin and proximity effect. In the skin effect the density of the current flow in a conducting wire tends to migrate toward the surface of the wire. Electromagnetic induction into these wires at times can cause opposition of current or resistance which turns into heat. This effect can be minimized by selecting a wire diameter sized that is smaller than the skin depth of the electromagnetic field.

When wires are packed together, as they are in stator slots, induced fields of the individual wires effect the surrounding wires packed next to it. This concept is known as proximity effect. Stray losses tend to decrease with increase with temperature where I^2R increase with temperature rise due to increased resistance.

Iron core loss is associated with material of the stator and can be broken down further to two subcategories known as hysteresis and eddy current losses. These losses

occur due to the occurrence of an alternating magnetic field passing through the stator core material. Interaction of the varying magnetic field with the magnetic iron material of the stator causes some intermolecular friction resulting in heat and thus power loss [17]. This is a hysteresis loss and the amount of this loss can be depicted by a hysteresis loop. Figure 1-8 shows an example of a hysteresis loop. This loop changes size based on the strength of the magnetic field and in turn the magnetizing flux. The equation that depicts this hysteresis loss is as follows:

$$P_{Fe} = \kappa B^n f^{\alpha} \tag{1.4}$$

where 'B' represents the magnetic flux density and α is an exponent that typically has values between 1.8 and 2.2. The variable f is the frequency in Hz of the machine with coefficients κ and α representing coefficients of conductivity, lamination, and thickness of laminations of the stator core [18]. As seen from the equation as a PM motor machine reaches higher speeds, the accuracy of the coefficients becomes more critical. Eddy currents are circular currents that occur from being induced by an alternating magnetic field [19]. The currents cause power and then turn into heat. If the frequency of the machine is small then the effects of these currents is negligible but if frequency is higher for accuracy of the design it is necessary to calculate.

To represent total stator loss a combined equation of hysteresis, classical eddy current and excess eddy current is shown below:

$$P_{Iron} = \kappa_h B^n f^{\alpha} + \kappa_c (Bf)^2 + \kappa_e (Bf)^{3/2} \tag{1.5}$$

where K_h, K_c, and K_e represent respectively the coefficients for hysteresis, eddy current, and excess eddy current. Other than these coefficients the only difference from Equation 1.3 are the exponent values are specified in the classical and excess eddy current losses. In the case of higher speed machines the calculation methods of core loss become a little more involved. Finding the right material for the stator core is very important for design characteristics. Ideally to fully optimize a motor design that contains high power density and high torque capability the stator material would contain high flux density saturation to decrease volume, weight, and losses as well as high permeability for less reluctance [17]. However, there is no perfect material and the design tradeoffs consist of finding good flux saturation with low iron core loss.

The rotor also experiences loss due to eddy currents induced in the shaft and permanent magnets. There are three different considerations for eddy currents in the rotor. With no load on the rotor there will be eddy current effects to fact that there are slots in the stator contributing to the alternating magnetic field effects. When the rotor has load the windings of the stator have induced harmonics that cause loss. Finally, time harmonics due to pulse wave modulation (PWM) cause loss as well at load. To reduce these effects you can make slot openings smaller, create fractional winding, and put line inductors to filter out higher order harmonics in the PWM. Increasing the switching frequency of PWM can also reduce the loss [17, 18].

The last loss to consider is windage loss. This loss occurs due to temperature increase of the fluid between the rotor and the stator due to shearing of the fluid. This fluid is generally ambient and during high speed operation can have a significant

contribution to overall inefficiencies. The dependents of windage loss in the motor are the rotation speeds of the shaft as well as properties of the fluid such as temperature and pressure density [17].

Motor design tradeoffs require a detailed analysis of the overall losses in the system. These losses can reveal areas of inefficiency and also areas that can be compromised for more desirable characteristics in the bigger scheme of things. Reliability and performance are always a priority in the design. The accurate analysis of losses within a system allow for design flexibility.

1.7 Thesis Organization

In Chapter 2 the design for a multi-pole PM motor will be described in full detail. The design relies on magnetic circuit analysis, which provides fundamental design equations. The method for design and solving for unknown parameters has been implemented using MATLAB. The code previously developed for two pole PM motor at UCF (PM Motor Designer) has been updated to account for multiple magnetic poles for surface mount magnets on the rotor in this thesis. The PM Motor Designer provides the design solutions which are used as inputs into ANSYS RMXPT. From this software, our design is verified and optimized by examination of efficiencies and design curves.

Chapter 3 provides a voltage control scheme to drive the design. Integrated electrical simulation results of the motor and controller to follow highly dynamics flight profiles are provided to show the stroke tracking, input power (including regenerative power), and winding copper loss.

In Chapter 4, experimental work at the Air Force Research Laboratory (AFRL) at the Wright Patterson Air Force Base (WPAFB) will be discussed. At AFRL, numerous tests and experiments are being conducted using a developed setup of an MTS Hydraulic press. The work done is testing and evaluation of a lower power motor through system integration. Motor design considered in this thesis is a design that hopes to be implemented in the future, but is not the same motor used in experimentation. This process provides experimental data to validate motor models. Even though the proposed motor design is not used in experimentation the conclusions drawn from this experiment will be helpful for future implementation. Experimental setup of the press, testing procedures, and results will be presented. Experimental uncertainties will also be studied.

In Chapter 5, conclusions are drawn from the entire scope of this project includes electric motor structure design, voltage controller design, and experimental considerations.

CHAPTER TWO: PM MOTOR Design

2.1 Introduction

The goal in this chapter is to create a generic PM motor design method and tool that can later be manipulated for a wide variety of multi-pole designs. The design chosen here is a 10 hp, 10krpm PM motor. Generally a four pole design is more common in a PM motor for EMAs. There is a limit to the amount of poles a motor can efficiently be used. This will be discussed in further detail in the later sections of magnetic circuit modeling and optimization [19].

In electric motor design there is a large amount of parameters dealing with electrical/mechanical relationships, magnetic circuit modeling, as well as materials. Due to the large amount of parameters, there are many design tradeoffs. Design is generally a constant battle between efficiency and cost. With this in mind, the relationships made for this specific design will consider both reasonable costs with optimal efficiency.

As described above there are many fields of science involved in the determination of the highest efficiency for an electric motor. It is not the intention of the paper to go into too much detail in all of these areas. Deeper understanding of the electrical and magnetic descriptions will be provided for strict purpose of showing newly derived equations for the specified motor design of the project.

Properly defining the use and performance of the motor is key to the optimization and determination of proper design parameters. The first step in optimization will be to use the fundamental knowledge in all areas of motor design to come up with as many

design parameters as possible given certain specifications. Once a sound design is made based on these parameters, different numerical techniques, such as FEM or design curves can help to further optimize the design. The methodology used for parameter determination and numerical analysis will be described in detail.

2.2 Multi-pole PM Design

2.2.1 Design Methodology

Since a motor design was needed for the simulations before there were any real geometries, a software package that automatically dimensioned a motor based on given performance specifications was designed. This PM motor designer gave all the geometries. This process involves taking in some known for example input parameters such as output power, terminal voltage, number of poles, mechanical speed, number of slots, a few options for slot type, coefficients for the properties of the steel, etc.

Traditionally, in order to fully understand the relationships made through motor design a great deal of background is needed in the development of magnetic circuit modeling and electrical as well as mechanical relationships. Rather than describing this background leading to the design equations, this specific PM design methodology will be used and fundamental equations can be explained in the process. This design methodology is the basis for the PM design created in MATLAB to quickly calculate sizing equations based on known input values. Therefore, this process will give a basis for the PM design code.

The best way to show the process of motor design is to break down and summarize various sections of design explaining the derivations of these equations and the assumptions that were made in the design process. The most important things to remember in the motor design are understanding specifications and limitations of the design, using as many fixed equations or given values as possible, and solving for the unknowns in the correct order. There are many approaches to design and a lot has to do with initial assumptions and tradeoffs that are made.

The approach described will begin with the specification of the motor used to specify some constraints. Mechanical design of the motor is relative to the sizing. The challenge of the mechanical design of the motor is seen as the power level is increased. Sizing equations will be the initial basis for the design. The sizing equations include volume equations for the stator indicating diameter and length based on the amount of torque required. Rotor diameter and length equations are also initially derived. Values such as rated speed, rated output power, number of poles, number of slots and a few others are examples of fixed equations to help with sizing calculations. For this motor, the specifications are as follows:

Performance Specifications	Value
Ouput Power	10 hp or 7460 W
Terminal Voltage from Wall Outlet	270 V
Mechanical speed	10 krpm
Number of Slots in Stator	24
Input Voltage Configuration	Y - Connected
Number of Permanent Magnets	4
Fractional Stator Pitch	5/6
Number of Slots in Stator	24
Samarian Cobalt Residual Flux Density	11.3 kG
Samarian Cobalt Coercivity	9.5 kOe
Estimated efficiency	0.95
Power factor	1
Percent Overspeed	0.2
Magnet embrace	1
Slot Style	Box type, Tight mouth box type, Wedge
Hysteresis loss coefficient	0.0047
Eddy current loss coefficient	0.0001
Excess eddy current loss coefficient	0.0000058
Air friction coefficient	0.001803041096839

Table 2-1: Performance Specifications

With these specifications, some parameters can be quickly calculated. First the number of slots is determined by

$$n = \frac{N_s}{3p} \tag{2.1}$$

where N_s represents the number of stator slots, and 'p' is the number of poles. This number must be a whole number greater than zero and represents the number of groups. Phase voltage can also be calculated easily. A wye network is used in this design which is calculated by taking the terminal voltage and dividing by $\sqrt{3}$.

At the beginning of the design, the maximum rotor diameter needs to be calculated:

$$D_{r\max} = \frac{v_r(length/\min)}{1.2n_m(rev/\min)\pi} \tag{2.2}$$

where v_r represents the design limit or max peripheral speed of the rotor based on present day steel alloys. The max peripheral speed is 35,000 ft/min in this design. The value of n_m is the mechanical speed which is one of the fixed parameters rated at 10 krpm. This equation can also be used as a final check for the rotor size limitations.

The next pertinent sizing equation is given by

$$\frac{D^2L}{\tau} = V_o \tag{2.3}$$

where 'D' is stator bore diameter and 'l' is the length of active region. The torque is represent by τ, which is determined by the output power divided by the rotational speed. The essence of this equation is to explain how big the motor size must be in order to create a required torque. V_o represents the inverse of the current density and depends on the cooling method. The cooling method is determined by the output power of the motor.

If the motor is 10 hp or less, air cooling is used; and for motors above this, water cooling is used. The cooling for this motor is therefore air and the coefficient is 9.5 $in^3/(ft.lbs)$. Another consideration to be made is that if the length of the motor is considered equal to the bore diameter then the diameter can be estimated by the following equation:

$$D = (\tau V_a)^{\frac{1}{3}} \tag{2.4}$$

This assumption is made based on some basis physical principles. If diameter is much larger than the length, the motor will have very high inertia. If the motor length is much longer than the diameter a sort of baring effect will occur. The initial sizing equations used are needed to provide some general values so that the design process can be completed. It is not until the end of the simulation till some of these equations get refined. This method references some of the initial assumptions that must be made in order to get a design solution. More of these estimations are made in this section of the design.

One of these assumptions initially made is the stator outer diameter which is estimated to be 1.6 times the stator bore diameter. It is not until the precise slot dimensions are solved later in the design that the accurate values for the stator bore will be calculated. Now that the outer diameter for of the stator has been estimated, the area of the stator, stator iron, volume of the iron and mass of the iron can be calculated as a result. The estimated mass of the iron will be used for estimations of core loss. This includes the hysteresis, eddy current, and excess eddy current loss.

In order to deal with some of the remaining sizing equations, calculation of stator winding factors must be made. These equations deal with the slot pitch, coil pitch, and coefficients for back EMF calculation. A major advantage to fractional pitch is the reduction of cogging torque. This is a parasitic value of torque that is characterized by the ripple in the torque of the motor. The slots per pole per phase in the propose motor is described by 24 slots divide by the number of phases, 3, and the number of poles, 4. The result of this means there are two slots per pole per phase. When this value is greater than one there are disadvantages and advantages. The disadvantage is that if this number increases individual slot areas are decreased indicating a decrease of ability for electrical loading [19]. The advantage is the smoothing of back EMF in the stator by creating wider spreads of the windings for a specific phase over the stator. Slot pitch is a fixed equation given based on the number of slots between slot windings dividing by the number of slots per pole.

Slot pitch in electrical angle is defined as

$$\gamma = \frac{\pi \cdot p}{N_s} \tag{2.5}$$

Here the number of poles divided by the stator slots multiplied by π will indicate a fractional pitch whose number is not whole. Similarly, coil pitch in electrical angle is also calculated by

$$\rho = \pi \frac{N_m}{N_p} \tag{2.6}$$

where $\frac{N_m}{N_p}$ represents the stator pitch given in the fixed equations and described previously. Another relation is the skewed angle in electrical radians given by

$$\zeta = \frac{l\zeta_m}{r_{si}} \frac{p}{2} \tag{2.7}$$

where 'l' represents the length of the motor, ζ_m is the mechanical skew set to zero by the fixed equations, r_{si} is the stator bore radius, and again 'p' is the number of poles. The coefficients from (2.5) to (2.7) can then be used to form the motor winding factor k_w [19].

Coils of a motor are related to the winding structure in the stator slots. The inputs to this motor take in three phase voltages. Therefore, each phase belongs to one winding group. Multiple windings around particular slots make up a coil. The interaction of one motor pole and one group of windings is called a group [19]. There are numerous ways to configure a winding structure in a motor. The main constraint that dictates winding type is size. Some of the style configurations are single layer lap, double-layer lap, and single-layer wave. The details of these configurations are not necessary to elaborate on, simply now that these configurations have an effect on flux linkage, inductance, which thus leads to force and torque.

Flux linkage and inductance of the stator core are the fundamental concepts of coil and winding structure. In the stator the flux that occurs is due to the current passed

in the stator windings. There are multiple turns of copper wire that make a winding in a stator slot and the total flux created by this winding is considered the flux linkage. The flux is represented as

$$\phi = \frac{NI}{R} \tag{2.8}$$

where 'N' is the number of turns, 'I' is the current, and 'R' is the reluctance. Thus the flux linkage can be defined by

$$\lambda = N\phi \tag{2.9}$$

where 'N' is the number of turns and ϕ is the total flux create by one turn. It is also common to define flux linkage and current in terms of inductance. Due to the fact that the stator contains multiple slots and multiple sources of magnetic excitation mutual and self inductances are important concepts to consider. Self inductance is described as the number of turns and amount of flux created in a winding on itself. Mutual inductance describes the mutual coupling of inductances between two or more coils.

The number of effective turns per coil can be calculated by the following equation:

$$N_c = \frac{1.1V_{\phi rated}}{2\sqrt{2}\pi f_e n k_w B_m D l} \tag{2.10}$$

where $V_{\phi rated}$ is also the calculated phase voltage. The electrical frequency, f_e, is simply the given mechanical speed multiplied by the number of poles divided by two. As mentioned previously the number of groups that are affected by one motor pole is described by n. The back EMF due to stator pitch is indicated by k_w. The net magnetic field, B_m, is a result of the residual flux density B_r of the Samarian cobalt permanent magnet. Again the estimated diameter of the motor is depicted by' D', and the length of the motor l.

Similarly the effective turns per phase is calculated by

$$N_{eff} = \frac{pnN_c k_w}{1.1} \tag{2.11}$$

Rated voltage, power input, and current can also be calculated based on slot characteristics if not given as a fixed equation. In this design rated voltage was given. Calculation for rated phase voltage can be described as:

$$V_{\phi rated} = \sqrt{2}\pi f_e N_{eff} \phi_m \tag{2.12}$$

The only variable in Eq. 2.12 that has not been explained is ϕ_m. The flux density per magnet is described by ϕ_m:

$$\phi_m = \frac{2B_m Dl}{p} \tag{2.13}$$

Power input can also be initially estimated to help with initial current rating values, and later recalculated more accurately based on current density limits and slot parameters. In this design the power in is initially used by estimation of power efficiency. This efficiency is another assumption that is made in order to complete this specific design process. The efficiency of the motor is estimated to be 95%. To determine the input power all we need to do is take the given output of the motor and divide by the efficiency.

To accurately calculate power input the relation, the following equation is used:

$$P_{in} = 3V_{\phi,rated} I_{A,rated} \cos\theta \tag{2.14}$$

which only requires explanation of $I_{A,rated}$ and the power factor because $V_{\phi,rated}$ was already described in Equation 2.12. Equation 2.14 can be simply rearranged to solve for $I_{A,rated}$ by the estimation of P_{in}.

On the other hand, we can obtain

$$I_{Arated} = \frac{d_{s1}\pi D r_s}{2N_c N_s} J_s \tag{2.15}$$

This equation is based on slot geometries as the area of the slot determines how much current can be passed into the motor. The slot depth is described by d_{s1}. The variable r_s is a ratio of the slot geometries $\frac{b_s}{\lambda_s}$. These geometries are seen in Figure 2-1.

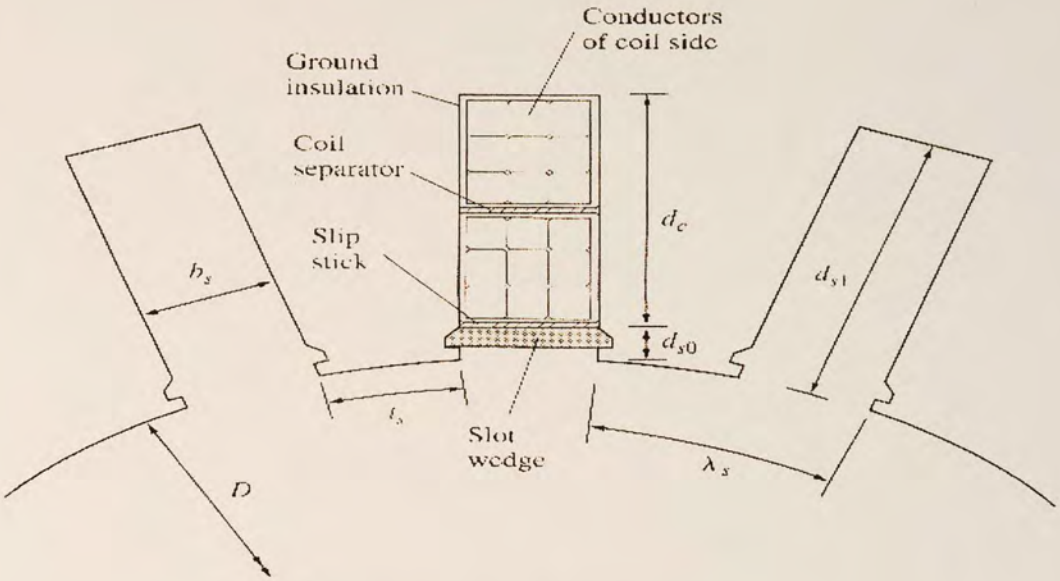

Figure 2-1: Stator Slot Structure

The current density J_s is also a factor of current rating. This will give another gauge on how the slot structure will be configured. It is important to determine the area of the slot occupied with conductors or coils to ensure sufficient area in the conductor for cooling. From the calculation of the diameter of each wire to the insulation of the wire around it, it is necessary to know and create a margin of the area for cooling. These calculations are considered in this design for both an air cooled and water cooled case. However, air cooled is the obvious choice for this design.

The limitations of the diameter of the wire are based on the current density limit. A minimum of 50 gauge wire was used in the designer and the max diameter was taken between the two. Based on the diameter of the wire wrap and conductor the total area of the wire area is calculated. Based on this area and the number of turns the total are is calculated. The margin area required for proper air cooling used was 23%.

Slot design is the next area of calculation. There a few type of slot styles configured for this design method. In the PM motor designer code a dimensioned image of one slot in the particular design to give a quick determination if the design is reasonable. It also allows currently for two types of slot geometries. The two slot structures are a rectangular or box type. One has an open mouth structure and the other is a narrow tooth structure. The benefit of narrow mouth is the reduced eddy currents in the permanent magnet and rotor shaft. Seen below are the two types of slot structures offered by the PM motor designer.

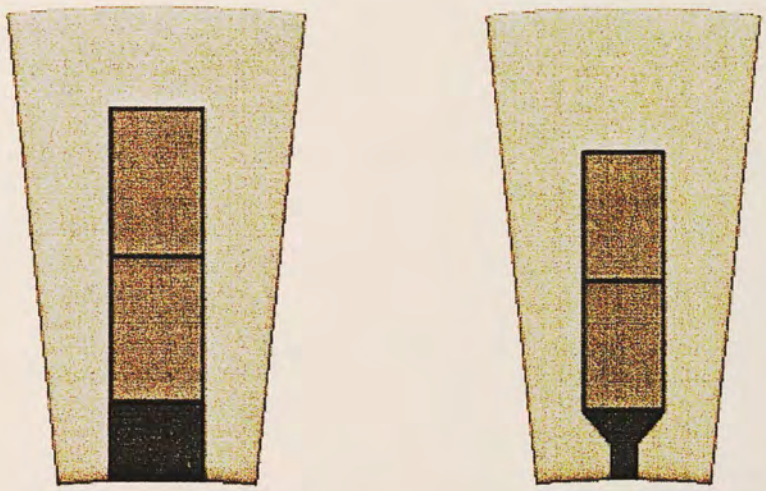

Figure 2-2: Stator Slot Dimension from PM Motor Designer (left) Wide Mouth Box Type (right) Narrow Mouth Box Type

These two geometries are dimensioned based on max widths and conductor area specifications that were described previously. Slot lining is constructed for insulation from the stator walls and a way to separate coils. Narrow mouth can also make the magnetic field in the slot more uniform reducing cogging torque. A third type of slot structure has recently developed in designer helps increase the design options and

contributes to another motor design used for the experimentation section. This slot design is called wedge type. The characteristics of this design as seen in Figure 2-3 have parallel teeth and thus a maximum slot area. Due to this maximized slot area the back iron width can be reduced and allow for an overall smaller volume of the motor. The maximized slot area can also allow for extra space for cooling of the copper windings. As a result a reduction in volume creates a higher power density. Wedge type slots seem like the most promising style for this reason however the winding structure has not yet been determined.

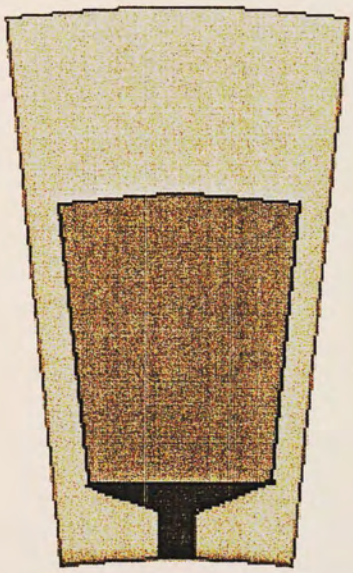

Figure 2-3: Wedge Style Slot Design

The dimensions for the calculation of the wedge slot were based on the diagram in Figure 2-4.

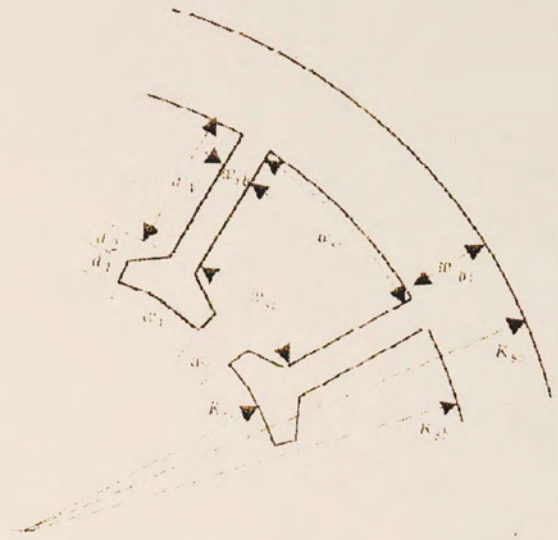

Figure 2-4: Slot Geometry for Wedge Slot Design [19]

Once these slot dimensions are determined and the size is reasonable accurate values for stator outer diameter are calculation as well as the total volume. The stator outer (core) diameter is give by

$$D_o = D + 2S_d + 2(\lambda_s - b_{s0}) \tag{2.16}$$

where D represents the bore diameter, S_d is total slot depth, λ_s is the arc length of one slot structure, and b_{s0} is slot width. Total volume of the motor is next calculated with this new more precise motor diameter as

$$V = \pi\left(\frac{D_o}{2}\right)^2 l \tag{2.17}$$

This is a simple volume equation and now sets the specifics to the outer measurements of the motor. The inner measurements of the rotor magnet dimensions and airgap are the next design procedure. A very critical derivation to the design scheme was the calculation of the airgap to accommodate a multi-pole configuration. Understanding magnetic field distribution inside the motor can be solved analytical through simple geometries. In order to get very accurate analysis of the distribution, FEM is generally used. This method converts the motor in discrete points were individual electromagnetic field distributions can be calculated. Many basic magnetic circuit relationships and magnetic concepts were previously discussed in chapter one under the motor materials and the losses section.

These concepts included explanation of the BH hysteresis loop of a permanent magnet, permeability, and the different types of losses in a motor design. The permeance across the airgap is critically to overall motor efficiency. The permeance, or ability for magnetic flux to flow in a material, across this airgap is part of this modeling. Reluctance in a magnetic circuit is simply the inverse of the permeance also considered magnetic resistance. This magnetic resistance occurs due the varying permeability that magnetic flux must travel through.

On the stator there are stator slots with slot openings. When considering airgap permeance the interaction of flux at this opening must be taken into account. There is less permeability thus higher magnetic resistance at this opening that the actual nonmagnetic material of the stator. The accurate modeling of the permeability in the slotted regions is designated by the geometry of the slot and the geometry of the permanent magnet.

The derivations made for the original PM Designer were written based on the fundamental magnetic equations for a two pole case. The modifications made were more than two poles on the rotor, surface mounted magnets, the improved air gap calculations using better magnetic circuit equations, more efficient back iron thickness calculations, and for approximate eddy current, windage, and hysteresis losses. The derivation of the airgap equation is based on the minimization of the magnet aspect ratio:

$$l_m/(\alpha_m \tau_p) \tag{2.18}$$

where α_m is the magnet fraction, and τ_p is the total width of the magnet. Figure 2-5 gives a general depiction of magnet size and shape.

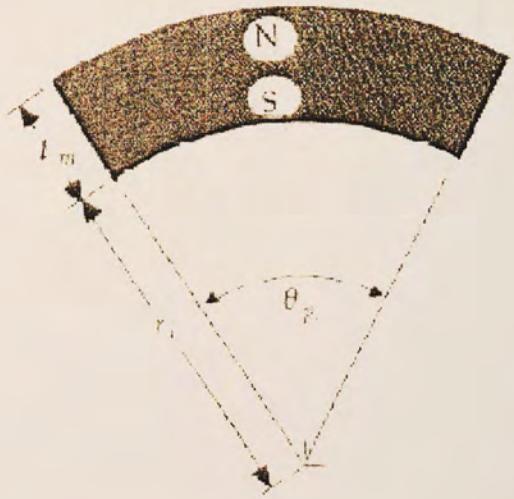

Figure 2-5: Arc-shaped Permanent Magnet [19]

In a practical design the magnet width is generally four times as large as the length or less. The final component to finding an optimal airgap length for multipole

cases is the dimensions of the rotor and airgap. Using these three relationships an effective airgap was derived for this case. This equation is derived based on the working point of permanent magnets described by the BH curve. Another relation we must make is the BH curve for the optimal static operating point of the motors BH hysteresis curve. In Figure 2-6 the variables used in the calculation of effective airgap for the multi-pole configuration are seen from magnetic circuit analysis:

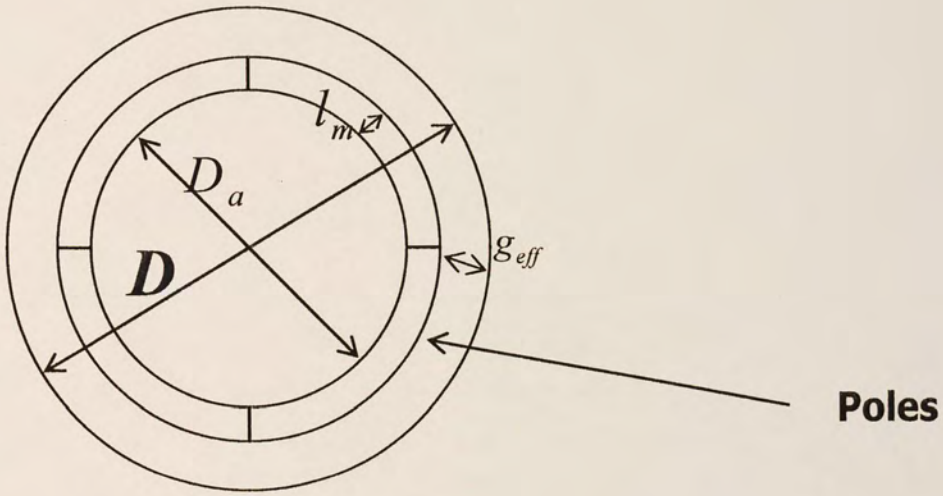

Figure 2-6: Multi-pole Diagram for Effective Airgap Calculation

$$g_{eff}H_g + H_m l_m = 0 \Rightarrow g_{eff}B_{mR} + \mu_0 H_m l_m = 0 \tag{2.19}$$

where g_{eff} is the effective airgap. Simply taking the right side of the above equation, we get

$$g_{eff}B_r - \mu_0 H_c l_m = 0 \tag{2.20}$$

From cross section geometry of the motor, we have

$$2g_{eff} + 2l_m + D_a = D \tag{2.21}$$

Following the guideline of magnet length and magnet aspect ratio, we set

$$\frac{l_m}{e_{mbrace}(D_a\pi)/p} = 0.25 \tag{2.22}$$

By rearranging Equations 2.20, 2.21, and 2.22 and solving for the magnet length in 2.22 the effective airgap based on all the following known values can be achieved:

$$g_{eff} = \frac{D\mu_0 H_c \pi e_{mbrace}}{4B_r P + 2B_r \pi e_{mbrace} + 2\mu_0 H_c \pi e_{mbrace}} \tag{2.23}$$

where D is the stator bore diameter, H_c is the magnetic coercively, e_{mbrace} is the magnet embrace, μ_0 is the permittivity of air, and B_r is magnetic remanance. This derivation was critical for the upcoming multi-pole PM motor designer. Ultimately more poles increase the force generated by a motor. In order to fit more magnets on the rotor their widths must decrease. The negative result of this is the increase in magnetic leakage flux and in turn lower airgap flux density. This simply implies that there is a limit to the number of poles. The airgap g can be obtained from

$$g = g_{eff} / k_c \tag{2.24}$$

where the Carter's coefficient is defined as

$$k_c = \frac{\lambda_s (5g + b_s)}{\lambda_s (5g + b_s) - b_s^2} \tag{2.25}$$

Carter's coefficient takes into account the slot openings in the calculation of the airgap. Effective airgap does not does this so Carter's coefficient gives the more accurate value of the airgap based on slotting. The rotor diameter including the magnet is now determined by

$$D_r = D - 2g \tag{2.26}$$

where 'D' is the stator bore diameter and g is the airgap. From Equation 2.26 the inside rotor diameter is determined, followed by the length of the magnet. The velocity of the rotor is also easily calculated with the new rotor calculation. The figure below show the final sizing dimensions of the motor.

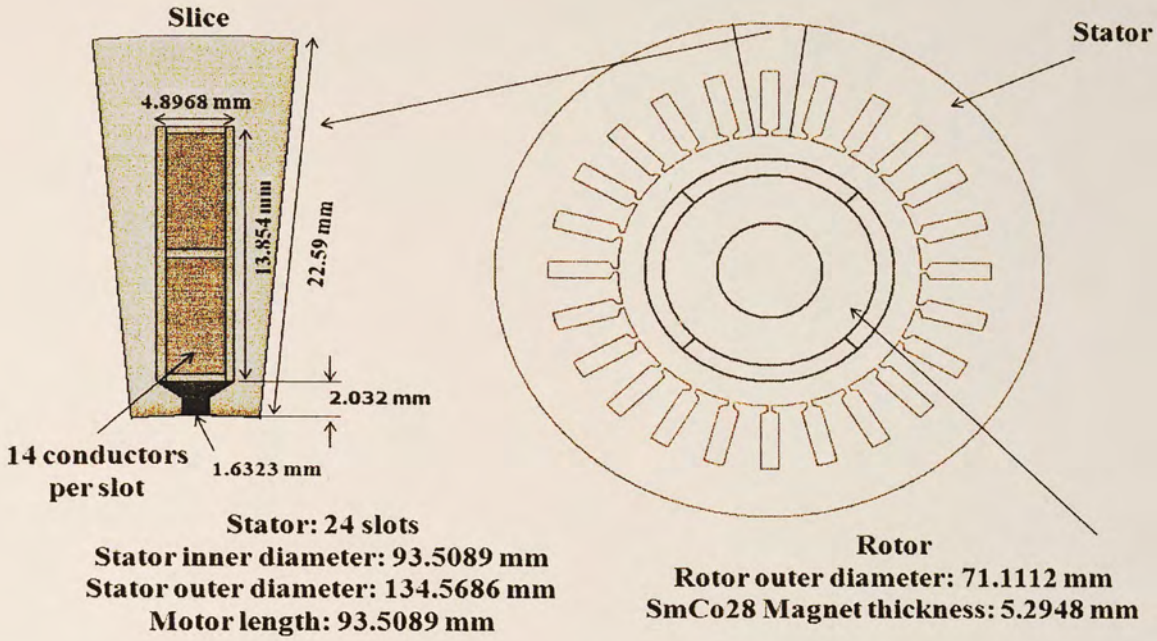

Figure 2-7: Final Sizing Dimensions of PM Motor

More accurate analysis of power loss can be made as well to estimate a better efficiency value of the motor. The equations describing the losses is in chapter one. An estimation of total loss is made by the combination of core loss, windage loss, copper loss, and friction loss. From this total power loss the overall efficiency of the motor can be determined. The PM motor designer is continually being upgraded as we go on, but at this point in time does provide a sound foundation for the parameters we need to enter into RMXPT. There is a conversion for the parameters to be input straight into the RMXPT straight from the PM motor design, which makes the transfer very simple and convenient.

2.2.2 Design Variations

The intended application of a motor is ultimately the deciding factor in which a PM motor is design. Again, there are so many design parameters and possibilities in which can help further optimize a design, but past insight in engineering helps us to explain some of the best methods for a particular design. Two of the most prevalent and common variations are in the rotor and slot designs.

Before describing these two variations it must be noted that the motor design will be of a radial flux topology. This meaning that the first rotor and stator are operating in the axial direction and that there is one airgap. This form of topology is most used today. Axial topology is characterized by two airgaps and generally will not be the type of motor used for EMAs.

When considering rotor structure there again is a wide assortment of configurations. The magnets can be surface mounted or internal to the core of the rotor. For this design we will use a surface mounted magnet structure.

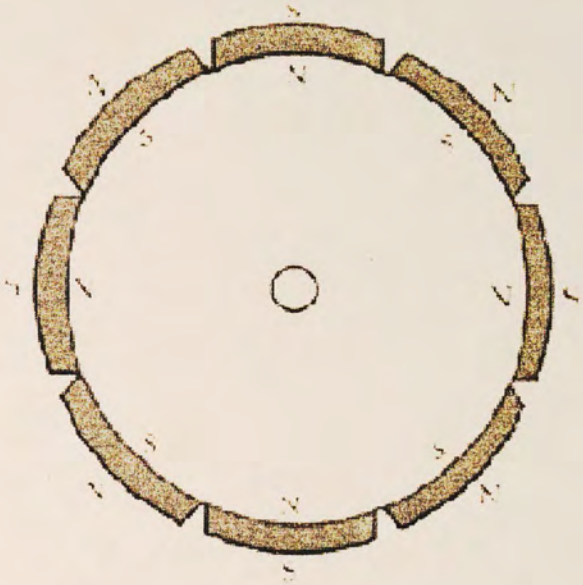

Figure 2-8: Surface Mounted Rotor Configuration

Cost is a major factor when deciding on a surface mounted structure. Eventually this motor design may be fabricated in the future this becomes a key factor. In Figure 2-3 the magnets follow a radial arc and can have either parallel sides or a bread loaf shape where the sides angle downward on the ends. Generally when the ends of the permanent magnet angle downward the cogging torque is reduced due to a much smoother transition from each magnet. The reasons for choosing other rotor configurations varies based on performance specifications and cost. The surface mounted structure will suffice for the design of this paper.

2.3 ANSYS RMXprt Simulation

RMXprt is an ANSYS's magnetics simulation software which can simulate and optimize an existing design. For the motor to be simulated in the ANSYS simulation

package, the values from our MATLAB PM Motor Designer must input into RMXprt. RMXprt will allow us to see efficiencies and design curves to determine if the design is sufficient. The parameters and values from the PM Motor Designer are directly translated to RMXprt.

```
Converted to RMXprt variables:
Machine:
   Number of poles        4
   Frictional loss       10
   Windage loss     34.4753
   Reference speed   10000
Stator:
   Outer diameter  134.0567
   Inner diameter   93.5089
   Length           93.5089
   Number of Slots       24
   Slot type              3
Slot:
   Hs0  1.016
   Hs1  1.016
   Hs2 7.9682
   Bs0 1.9666
   Bs1 5.8998
   Bs2 5.8998
   Rs        0
```

```
Winding:
   Winding layers                2
   Winding type         whole coiled
   Parallel branches             1
   Conductors per slot          12
   Coil pitch                    5
   Number of strands             1
   Wire wrap                0.0635
   Wire size (AWG)            13.5
   Slot lining              0.21997
   Wedge thickness            2.032
   Layer insulation         0.10999
   Limited fill factor         0.999
Rotor:
   Outer diameter 75.1112
   Inner diameter 32.2608
   Length         93.5089
   Pole type            2
Pole:
   Embrace              1
   Offset               0
   Magnet type      SmCo28
   Magnet thickness 5.2948
Shaft: non-magnetic
```

Figure 2-9: Values INPUT into RMXprt from PM Motor Designer

After these values have been input and transitioned to RMXprt the design can be simulated. Once the design is validated and there are no errors the statistical data can be viewed. This data includes all the parameters of the motor including output parameters when the motor has no load and when the motor is on full load. The full load solution data for our specified motor design is seen here as it is the most revealing data concerning efficiency of the design

FULL-LOAD DATA

Maximum Line Induced Voltage (V):	411.29
Root-Mean-Square Line Current (A):	16.7312
Root-Mean-Square Phase Current (A):	16.7312
Armature Thermal Load (A^2/mm^3):	263.642
Specific Electric Loading (A/mm):	32.8009
Armature Current Density (A/mm^2):	8.03764
Frictional and Windage Loss (W):	30
Iron-Core Loss (W):	0.00186389
Armature Copper Loss (W):	261.789
Total Loss (W):	291.791
Output Power (W):	7458.02
Input Power (W):	7749.81
Efficiency (%):	96.2349
Synchronous Speed (rpm):	10000
Rated Torque (N.m):	7.12189
Torque Angle (degree):	20.7183
Maximum Output Power (W):	19508.9
Torque Constant KT (Nm/A):	0.427377

Figure 2-10: Full Load Data of Simulated PM Motor Design in RMXprt

As seen in the data from Figure 2-9 the proposed design was able to reach a rather high efficiency level in RMXprt showing the design is sound. Figure 2-10 shows the efficiency rating as a function of mechanical speed. You can see that the efficiency starts to peak between 9000 and 10000 rpm PM motor showing that this is our most efficient operating speed.

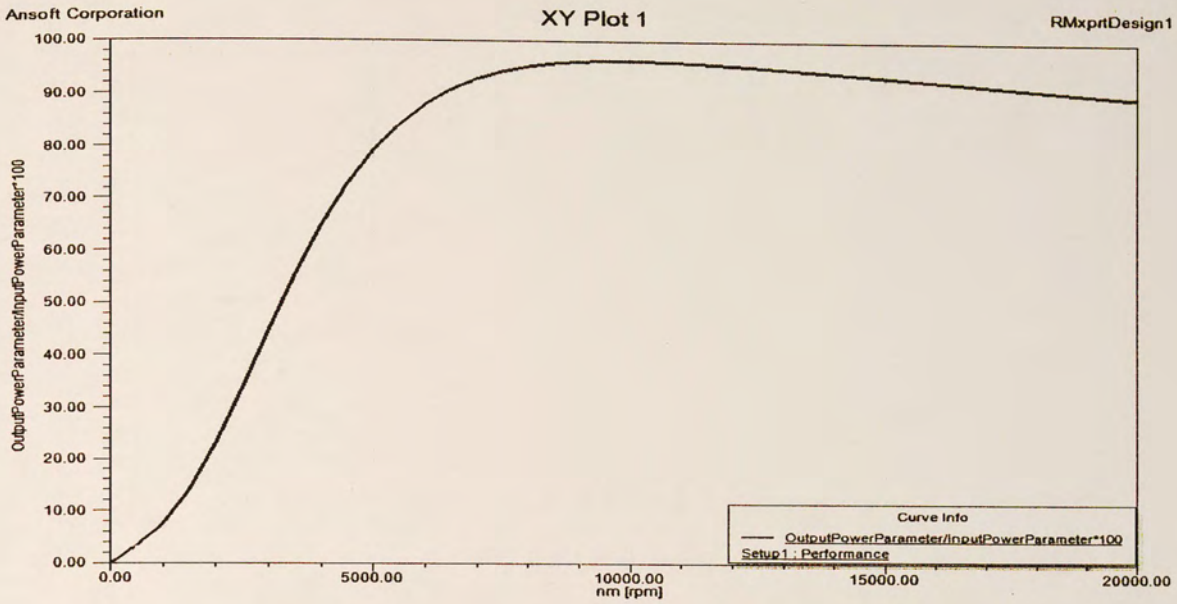

Figure 2-11: Efficiency vs. Speed of PM Motor

This relationship of torque angle and power in Figure 2-11 shows that the highest output power occurs when the torque angle is around 90 degrees.

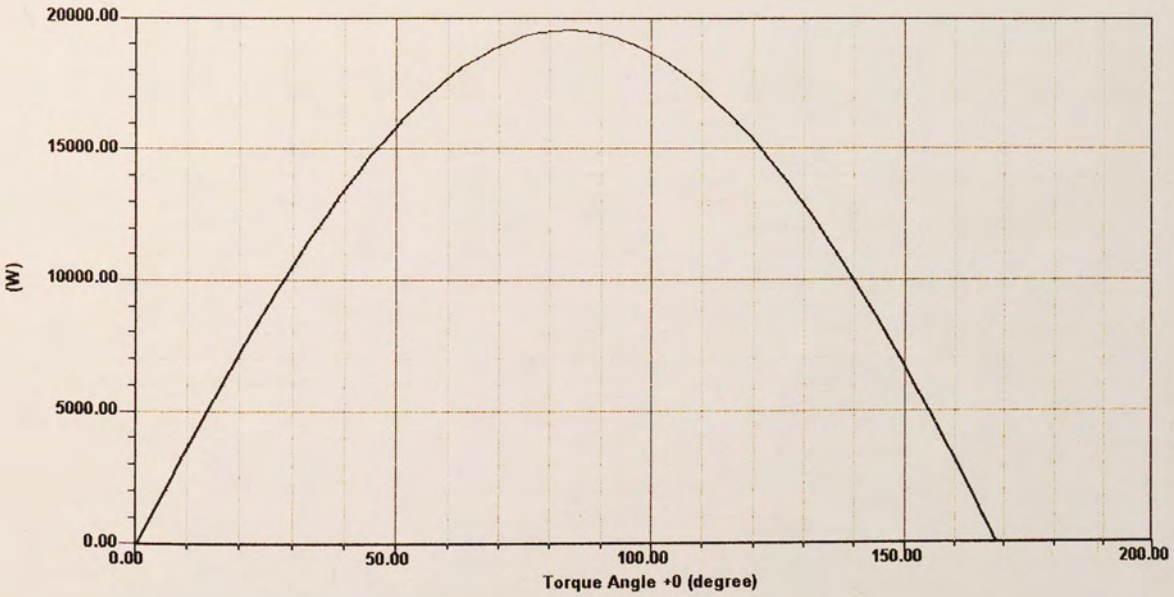

Figure 2-12: Output Power vs. Torque and of PM Motor

In Figure 2-12, we see the magnetic flux density in relation to electrical degrees. This shows the level of magnetic flux that is passed through the slot as the permanent magnet rotates around the stator.

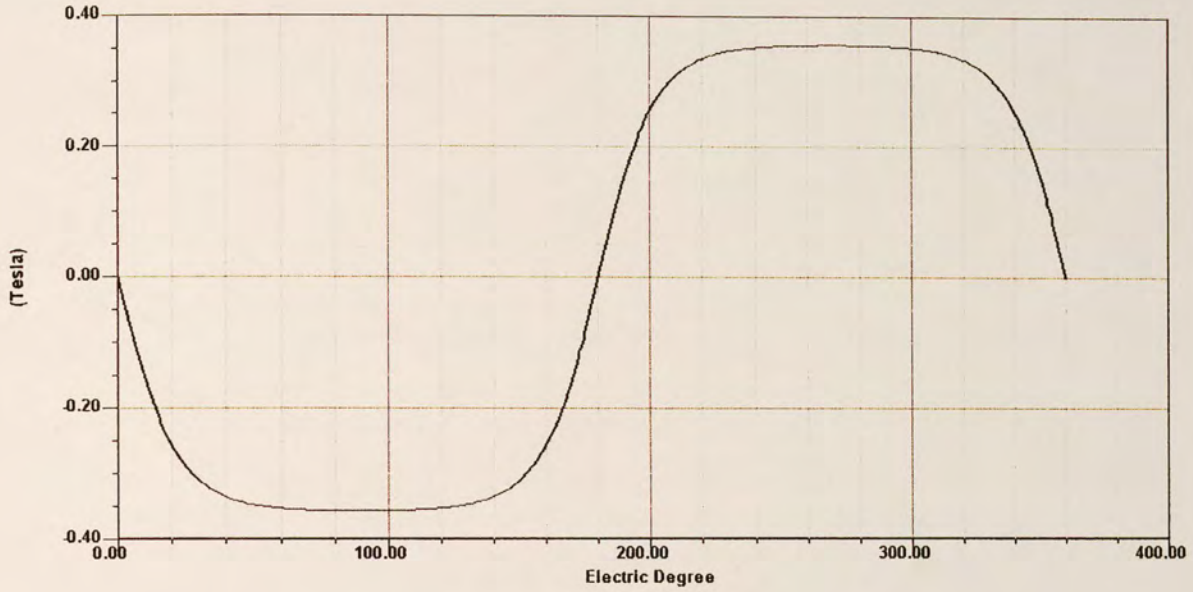

Figure 2-13: Magnetic Flux Density vs. Electric Angle

Although ANSYS software was used to validate the basic motor design, at this point the ANSYS software cannot perform all the tasks necessary to run a fully coupled thermal and EM simulation of a motor including all relevant nonlinearities. Therefore, although the ANSYS software was used, at this point, it is not seen it as a complete viable solution for the full EMA simulation making continued development of self-designed software key to future research.

RMXprt can also develop 2D and 3D geometries for the designed motor. The 2D and 3D geometries of our motor are shown in Figures 2-14 and 2-15.

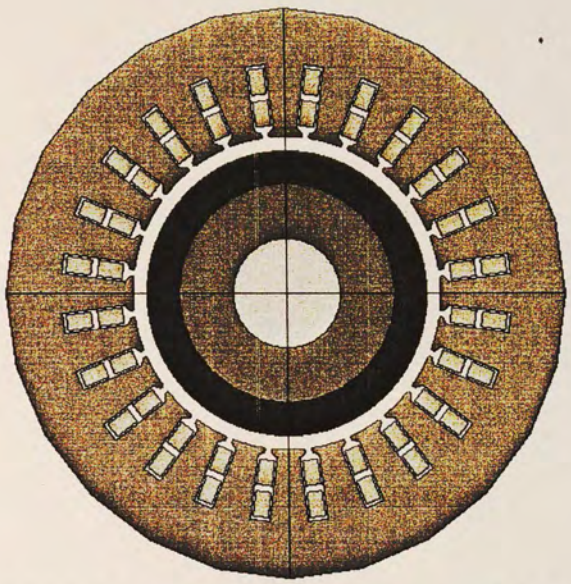

Figure 2-14: 2D Cross Section Geometry of the Design

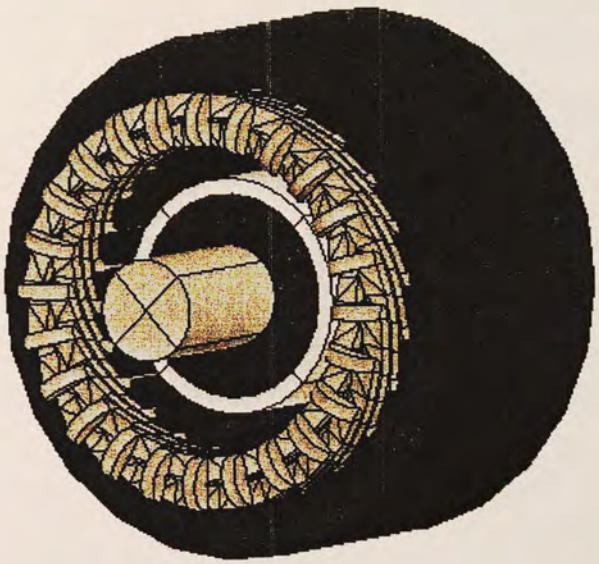

Figure 2-15: 3D Geometry of the Design

2.5 Conclusion

In this section equations were derived for multi-pole permanent magnet (PM) motor. From these equations, we updated the PM Designer software to include multi-poles. We then designed a 10 hp 10 krpm motor for an EMA. From simulating the motor through the Ansys software, this particular design was considered suitable. The efficiency was 95%. The same procedure for other PM motor designs will hold for various input parameters.

CHAPTER THREE: Dynamic Modeling and Control

3.1 Introduction

The control of the motor is critical in EMA system. When considering the highly transient nature of a military fighter aircraft, it is important that a motor is able to accurately follow the commands of the pilot. Many of the motors used in industry today are for steady speeds. It is much more challenging to design a control that has very dynamic control needs. When the speed of the motor is required to be ramped up and down frequently, the ability for dynamic control is necessary [5].

The type of control used in this thesis is voltage control. Proportional and integral gains are used to control quadrature voltage. By controlling quadrature voltage, the induced magnetic flux used to cause rotation or torque of the rotor is varied. The current creating magnetic flux that is in alignment of the rotor is called direct current. Maximum torque is produce from the current that is 90 degrees from the direct current called quadrature current. The transformations of three phase current or voltage and its benefits will be described in a later section. Since the direct current does not create torque for rotation, we set the desired direct current to be zero and design a controller to control the direct voltage with the direct current error.

A high resolution time stepping algorithm was used to predict next step values of the control for current, angle, and angular speed. In order to attempt to improve the speed of the solving dynamic equations to determine these values, second order and fourth order Runge-Kutta methods are employed. A comparison of these two explicit algorithms with implicit trapezoidal algorithm will be examined.

3.2 dq0 theory

When dealing with three phase balanced circuits calculations can become computationally demanding. Currents and voltages of the motor have a dependence on the rotor angle in the stator. Dq0 theory is a transformation that removes this dependence and turns three phase AC quantities into two DC quantities. Calculations are then performed using the DC quantities and then converted back using an inverse transform.

As described in Chapter 2, torque is created by the interaction of the rotor flux from the PM motor magnets and the induced magnetic field from the stator copper windings. Maximum torque in the motor occurs when the fields of the stator and rotor are 90 degrees from one another. Creating current in the stator that generates a magnetic field orthogonal to the rotor position is the highest efficiency as well. The new reference frame becomes relative to the rotor position. The figure below shows a representation of the dq0 reference pertaining to a two pole system.

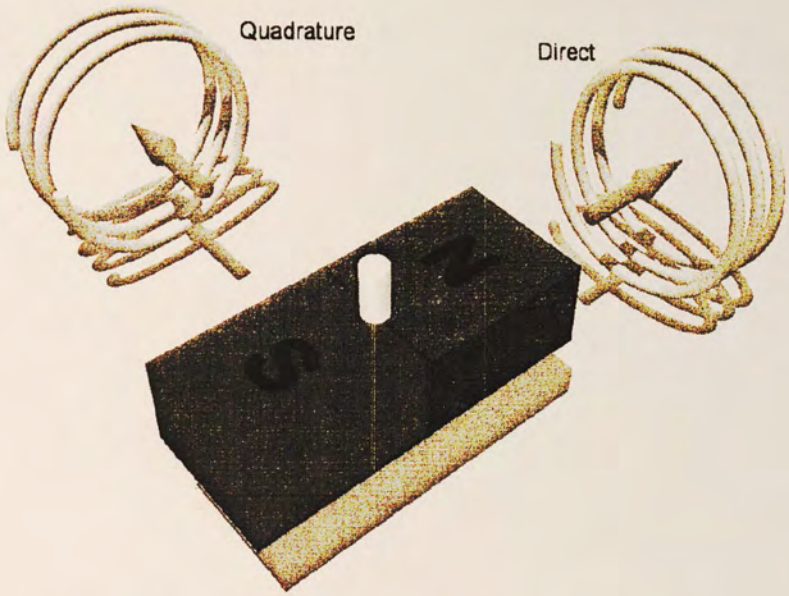

Figure 3-1: Representation of dq0 Reference Frame

One of the main reasons to doing dq0 transformations is to make the time dependent voltage and current equations, into time independent equations. Computational time is decreased significantly in a simulation that has very dynamic voltage inputs. The dq0 transform scripts will be described later with the control software. The transformation and inverse transform for a PM motor is denoted by the following equations:

$$\mathbf{s}_{dq0} = \mathbf{K} \cdot \mathbf{s}_{abc} \tag{3.1}$$

where

$$\mathbf{s}_{dq0} = \begin{bmatrix} s_d \\ s_q \\ s_0 \end{bmatrix}, \quad \mathbf{s}_{abc} = \begin{bmatrix} s_a \\ s_b \\ s_c \end{bmatrix} \tag{3.2}$$

Here s denotes voltage v, or current i, or flux linkage , etc. The transformation matrix $\mathbf{K}$ and its inverse are given as

$$\underline{\underline{K}} = \frac{2}{3}\begin{bmatrix} \cos(\theta_{me}) & \cos(\theta_{me}-120°) & \cos(\theta_{me}+120°) \\ -\sin(\theta_{me}) & -\sin(\theta_{me}-120°) & -\sin(\theta_{me}+120°) \\ 1/2 & 1/2 & 1/2 \end{bmatrix}$$

$$\underline{\underline{K}}^{-1} = \begin{bmatrix} \cos(\theta_{me}) & -\sin(\theta_{me}) & 1 \\ \cos(\theta_{me}-120°) & -\sin(\theta_{me}-120°) & 1 \\ \cos(\theta_{me}+120°) & -\sin(\theta_{me}+120°) & 1 \end{bmatrix} \tag{3.3}$$

where

$$\theta_{me} = \theta_m n_p \tag{3.4}$$

Here n_p is the number of pole pairs and θ_m is rotor mechanical angle.

3.3 Dynamic Equations

Dynamic Equations describe the dynamical nature of the motor. The motor dynamics are modeled by four primary dynamical equations in direct-quadrature reference frame (dq0): [20]

$$\frac{di_d}{dt} = \frac{1}{L_d}\left(-R_s i_d + n_p \omega_m L_q i_q + u_d\right) \tag{3.5}$$

$$\frac{di_q}{dt} = \frac{1}{L_q}\left(R_s i_q - n_p \omega_m L_d i_d - n_p \omega_m \lambda_{PM} + u_q\right) \tag{3.6}$$

$$\frac{d\omega_m}{dt} = \frac{1}{I}\left(\tau_m - \tau_L - c\omega_m\right) \tag{3.7}$$

$$\frac{d\theta_m}{dt} = \omega_m \tag{3.8}$$

where u_d is input direct voltage, u_q is input quadrature voltage, i_d is direct current, i_q is quadrature current, R_s is phase resistance, L_d is direct inductance, L_q is quadrature inductance, p is the number of poles, ω_m is the mechanical angular speed, θ_m is the rotor mechanical angle, λ_{PM} is the flux linkage from the permanent magnet, τ_M is the motor torque generated by the magnetic fields, τ_L is the load torque, I is the rotor's moment of inertia, and c is the rotor's coefficient of friction from windage and bearings. The magnetic torque can be obtained as:

$$\tau_M = i_q \left\{ \frac{3}{4} p \cdot \left[\lambda_{PM} + i_d \cdot \left(L_d - L_q \right) \right] \right\} \tag{3.9}$$

From (3.9), we find that when the L_d is equal to L_q which is the round rotor case, the magnetic torque is a function of quadrature current i_q only.

Even though to ensure optimal accuracy in power loss and temperature calculations a model of non-linear of motor parameters is needed, linear parameters of inductance and flux linkage are used in this simulation. Non-linear inductances based on current values may not be always necessary to get reasonable and revealing simulation results. This result is due to the fact the operating currents of a dynamic profile still produce inductance values in a fairly linear range.

L_d and L_q are not used as functions of i_q in this thesis. Direct current i_d does not contribute to the rotation of the rotor due to the optimal torque considerations. Therefore the control tries to maintain a value close to zero during operation [20]. Due to

the fact that most of the loss comes from the current and resistance through the copper windings this is the area of concentration related to linear inductance values. Even though core losses become more significant with increased motor speeds they still play a much smaller role than copper loss.

Setting the size of the time step in a simulation is critical to the speed. When a motion profile is used that is very dynamic or transient it is important to have a high resolution time step to capture all of these moments. Speed can be increased by creating a variable time step over a profile, but the fixed time step used for this control shows very little speed deficiency. In actual experimental implementation used for validation of models, variable time step is not an option so using a fixed time step will give more comparable. The advantage of a variable time step is the fact that the profile array can be smaller thus compressing the profile [20]. This technique uses low transient areas to increase the time step and high transient areas to decrease the time step. By using two loops, one macro loop used to step through the profile, and a micro loop used for the electrical equations that contain the variable time step based the frequency of the electrical time constant.

Built in MATLAB solvers used to determine next step values for the electrical equations have the disadvantage of not knowing the time step. Other methods of solving for the electrical equations are second order and fourth order Runge Kutta (RK) algorithm. This type of solver is an integration algorithm based on the calculation of trajectories. These two methods will not require a second micro loop used for the variable time step of the electrical equations. The hope is to improve speed in the simulation as loops tend to increase speed. There will be one macro loop for these implemented

solvers. A study and implementation of the second and fourth order RK method will be seen in the following section.

3.4 PM Motor Voltage Control

The control equations in the simulation use fundamental voltage control equations. Quadrature voltage represents the major contributing voltage to the torque of the motor. The desired quadrature voltage is indicated by u_q^* can be obtained by a PI controller as:

$$u_q^* = u_q + k_p e_{\omega_m} + k_i e_{\theta_m} \tag{3.10}$$

where the value u_q represents the quadrature voltage. The error in the angular velocity, e_{ω_m}, defined as the difference in the desired value of angular velocity and the present value $\left(\omega_m^* - \omega_m\right)$ is tuned by the proportional coefficient, k_p. As the error in the motor is compensated for with k_p there will be an accumulated error along the profile while the control is continually trying to compensate. This accumulated error is a function of the rotor angle error, $e_{\theta_{mc}}$. The error in rotor angle is defined as the difference in the desired value of rotor angle and the present value $\left(\theta_m^* - \theta_m\right)$. k_i is the integral tuning coefficient for this error.

Note that direct current and voltage has a desired value of zero so the control compensation is to keep these values as close to zero as possible. Therefore, the desired direct voltage can be obtained as

$$u_d^* = u_d + k_{pd} e_{i_d} \tag{3.11}$$

This equation consists of u_d which depicts the present value of direct voltage and the error in the direct current, e_{i_d}, which is the difference $\left(i_d^* - i_d\right)$ between the desired direct current i_d^* and the present value i_d. k_{pc} is a proportional compensation constant used to correct for the error in current.

The values in these equations that require tuning are PI coefficients. These values will be altered based on different motor parameters and profiles that are used in the control. When these values have been properly tuned, the currents, rotor angle, angular velocity, etc. can be calculated by solving dynamical equations using the voltages u_d^* and u_q^* as inputs.

In the following, we will discuss solution procedure of dynamical equations (3.5) to (3.8). We can define

$$\mathbf{X}(t) = \begin{bmatrix} i_d \\ i_q \\ \omega_m \\ \theta_m \end{bmatrix} \quad \text{and} \quad \mathbf{F}(\mathbf{X}(t),t) = \begin{bmatrix} \frac{1}{L_d}\left(-R_s i_d + n_p \omega_m L_q i_q + u_d\right) \\ \frac{1}{L_q}\left(R_s i_q - n_p \omega_m L_d i_d - n_p \omega_m \lambda_{PM} + u_q\right) \\ \frac{1}{I}\left(\tau_m - \tau_L - c\omega_m\right) \\ \omega_m \end{bmatrix} \tag{3.12}$$

And then re-write (3.5) to (3.8) as

$$\frac{d\mathbf{X}(t)}{dt} = \mathbf{F}(\mathbf{X}(t), t) \tag{3.13}$$

We can approximately write

$$\frac{d\mathbf{X}(t + \frac{\Delta t}{2})}{dt} \approx \alpha \frac{d\mathbf{X}(t)}{dt} + \beta \frac{d\mathbf{X}(t + \Delta t)}{dt} \approx \frac{\mathbf{X}(t + \Delta t) - \mathbf{X}(t)}{\Delta t} \tag{3.14}$$

Inserting (3.13) into (3.14) yields

$$\alpha \mathbf{F}(\mathbf{X}(t), t) + \beta \mathbf{F}(\mathbf{X}(t + \Delta t), t) \approx \frac{\mathbf{X}(t + \Delta t) - \mathbf{X}(t)}{\Delta t} \tag{3.15}$$

which gives

$$\mathbf{X}(t + \Delta t) = \mathbf{X}(t) + \Delta t[\alpha \mathbf{F}(\mathbf{X}(t), t) + \beta \mathbf{F}(\mathbf{X}(t + \Delta t), t)] \tag{3.16}$$

When $\alpha = 1$ and $\beta = 0$

$$\mathbf{X}(t + \Delta t) = \mathbf{X}(t) + \Delta t \mathbf{F}(\mathbf{X}(t), t) \tag{3.17}$$

which is the explicit Forward Euler Algorithm.

When $\alpha = 0$ and $\beta = 1$

$$\mathbf{X}(t+\Delta t) = \mathbf{X}(t) + \Delta t \mathbf{F}(\mathbf{X}(t+\Delta t), t) \tag{3.18}$$

which is the implicit Backward Euler Algorithm.

When $\alpha = \beta = \frac{1}{2}$

$$\mathbf{X}(t+\Delta t) = \mathbf{X}(t) + \frac{\Delta t}{2}[\mathbf{F}(\mathbf{X}(t), t) + \mathbf{F}(\mathbf{X}(t+\Delta t), t)] \tag{3.19}$$

which is the implicit Trapezoidal Algorithm or Crank-Nicholson Algorithm.

Runge Kutta (RK) is a family of algorithms that have a basis of using a taylor series expansion for approximating next step values [24]. This is an explicit algorithm that uses an implicit technique for intermediate steps. Explicit algorithms tend to be faster. The benefit of implicit algorithms is that there is a feedback type technique used, which generally translates into higher stability and accuracy. We will discuss second order and fourth order algorithms here. For second order RK Algorithm, we can write down

$$\mathbf{X}(t+\Delta t) = \mathbf{X}(t) + \Delta t \frac{d\mathbf{X}(t+\frac{\Delta t}{2})}{dt} = \mathbf{X}(t) + \Delta t \mathbf{F}(\mathbf{X}(t+\frac{\Delta t}{2}), t+\frac{\Delta t}{2}) \tag{3.20}$$

where

$$\mathbf{X}(t+\frac{\Delta t}{2}) = \mathbf{X}(t) + \frac{\Delta t}{2}\mathbf{F}(\mathbf{X}(t),t) \tag{3.21}$$

which is a half step explicit Forward Euler Algorithm.

For the fourth order RK algorithm, we neglect lengthy derivations. The explicit procedure is as follows:

Consecutively calculate the following

$$\mathbf{F}_1 = \mathbf{F}(\mathbf{X}(t),t) \tag{3.22}$$

$$\mathbf{F}_2 = \mathbf{F}(\mathbf{X}(t) + \frac{\Delta t}{2}\mathbf{F}_1, t+\frac{\Delta t}{2}) \tag{3.23}$$

$$\mathbf{F}_3 = \mathbf{F}(\mathbf{X}(t) + \frac{\Delta t}{2}\mathbf{F}_2, t+\frac{\Delta t}{2}) \tag{3.24}$$

$$\mathbf{F}_4 = \mathbf{F}(\mathbf{X}(t) + \Delta t\mathbf{F}_3, t+\Delta t) \tag{3.25}$$

And then taking the weighted average of **F**'s, we can obtain

$$\frac{d\mathbf{X}(t+\frac{\Delta t}{2})}{dt} = \frac{1}{6}(\mathbf{F}_1 + 2\mathbf{F}_2 + 2\mathbf{F}_3 + \mathbf{F}_4) \tag{3.26}$$

Finally, $\mathbf{X}(t+\Delta t)$ can be obtained from (3.20).

Now that second and fourth order RK algorithms have been explained the goal is to study the most efficient and effective method. Although, the results of all three methods will be ran to determine their statistics. The table below represents the results of each implemented integration algorithm ran with the same simulation program.

Integration Algorithm	Average Simulation Time of five minute profile	Average Simulation Time of one and a half hour profile
2^{nD} Order RK	8.3s	82.8s
Trapezoidal	10.3s	114.43s
4^{th} Order RK	20.5s	210.4s

Table 3-1: Integration Algorithm Speed Comparison

It is seen in the table that the 2^{nd} order RK algorithm is approximately 20% faster than the trapezoidal algorithm. It is over twice the speed of the fourth order RK in the five minute profile. When the simulation was run for an hour and a half the differences in speed become even more apparent. The speed of the 2^{nd} order RK is 25% faster than the trapezoidal method here. Another interesting thing to observe is that the implicit trapezoidal algorithm is faster than the fourth order RK method. This is mainly because that the explicit fourth order RK method needs four steps and the average iteration steps of implicit trapezoidal algorithm is about 2.5.

Now that the study has been complete the method used for the simulation will use second order RK algorithm. The simulation is run based on preexisting flight profile data and the motor parameters based on the 10hp motor. As a reminder linear inductance and flux linkage are used. The following results will reveal all the electrical aspects of the

output including mechanical stroke following of the actuator, mechanical torque following of load torque, direct and quadrature currents and voltages, as wells as values of winding power loss, and power in. These outputs will reveal the data necessary to determine whether the proposed motor and control is capable of following highly transient profile. Explanation of eight outputs from the simulation will be explained for an hour long mission profile.

3.5 Simulation Results

Figure 3-2 shows a one hour profile of an aircraft representing takeoff, normal flight, and landing. This output is a representation of altitude and will be the profile used to test the control of the proposed motor.

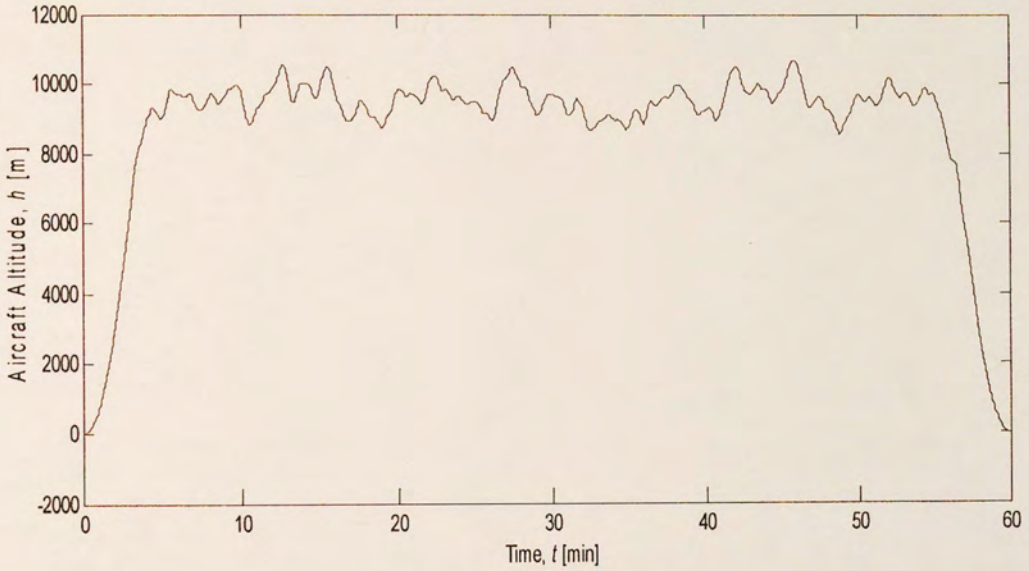

Figure 3-2: Altitude of One Hour Flight Profile

The desired stroke of one aileron actuator with respect to time is seen in Figure 3-3 over the entire one hour profile.

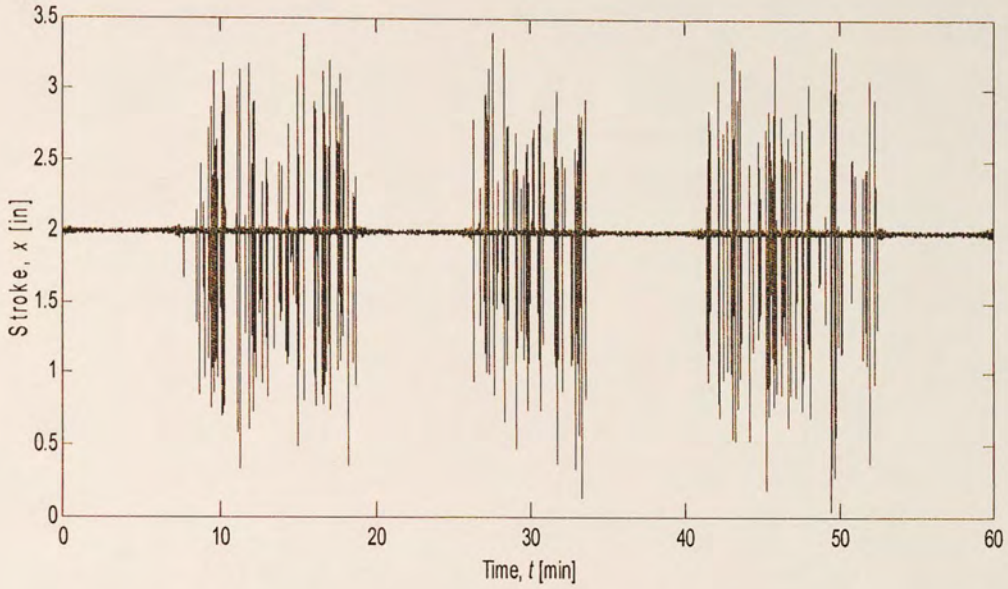

Figure 3-3 (a): Desired Stroke of Flight Profile

And the load force on the actuator over time is shown in Figure 3-3 (b).

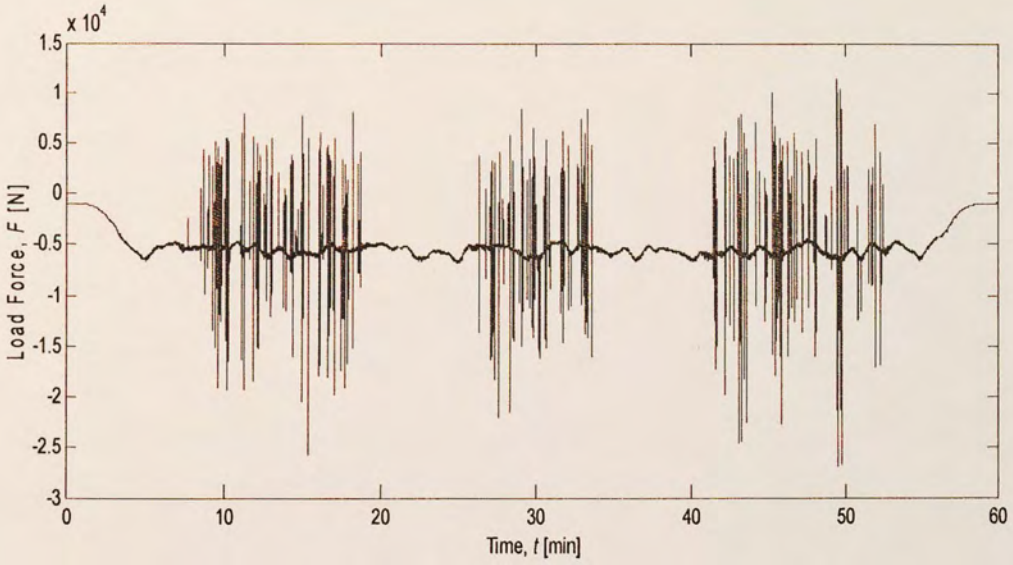

Figure 3-3 (b): Force of Actuator of Flight Profile

Figure 3-4 shows the stroke tracking of the voltage controller. The green line represents the actual stroke of the actuator based on the mission profile. The blue line is

the desired movement of the EMA shown in Figure 3.3. It is hard to see the blue because the green is covering indicating good control.

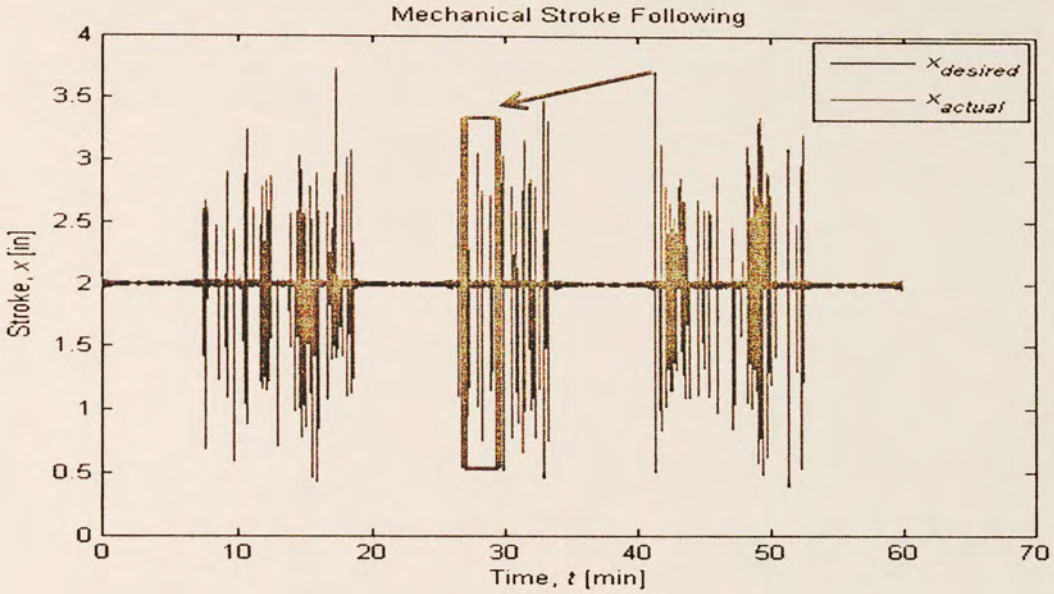

Figure 3-4 (a): EMA Stroke Profile

To further see the accuracy of the stroke following plot, the area of the blue square in Figure 3.4 (a) has been zoomed and shown below.

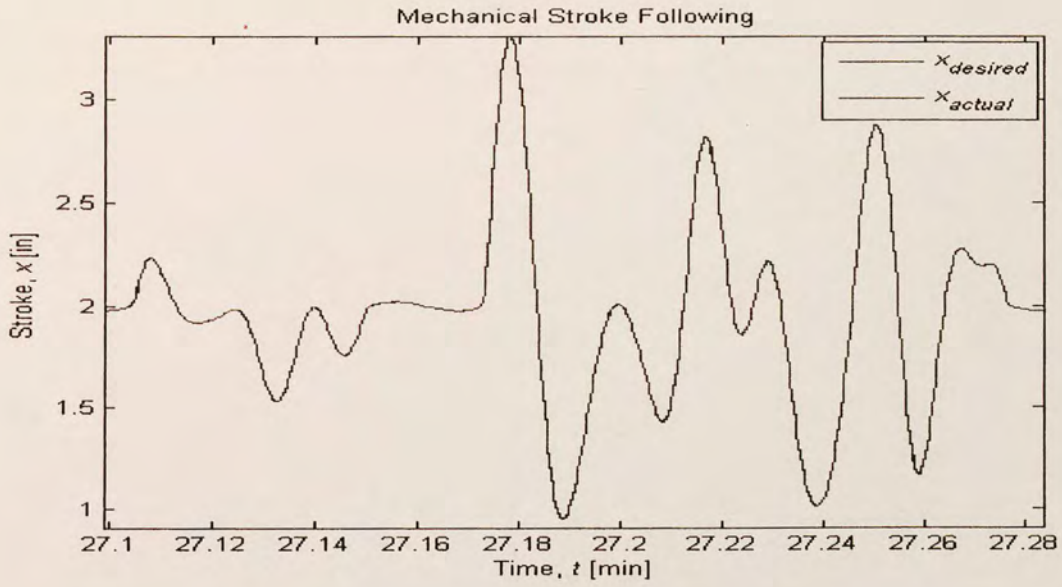

Figure 3.4 (b): Zoomed Section of Stroke Profile

The dq currents provided to the motor are shown in Figure 3-5. Notice that the current i_d nearly constant around 0 and doesn't exceed the dotted blue line limitations. This is a proper reading as direct current does not contribute to the rotation of the rotor. Only i_q contributes to the torque as seen by the variation in the green line. The dotted green lines represent current limits of the motor.

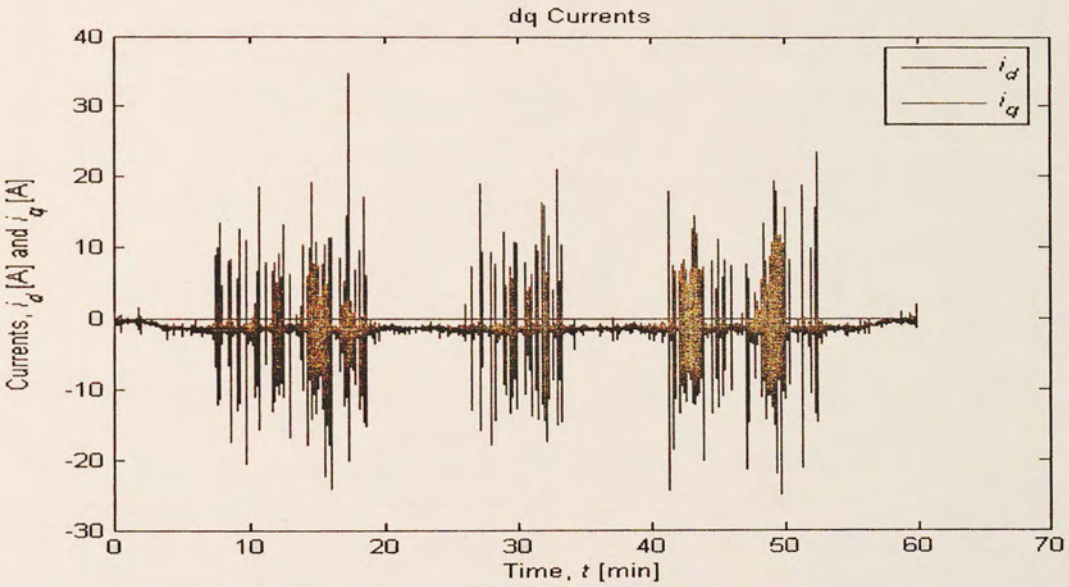

Figure 3-5: Direct and Quadrature Currents

The direct and quadrature voltages are shown here and similar to the currents. The direct voltage should remain around zero and the quadrature voltage should contribute to the requirements of the selected flight profile as shown in Figure 3-6.

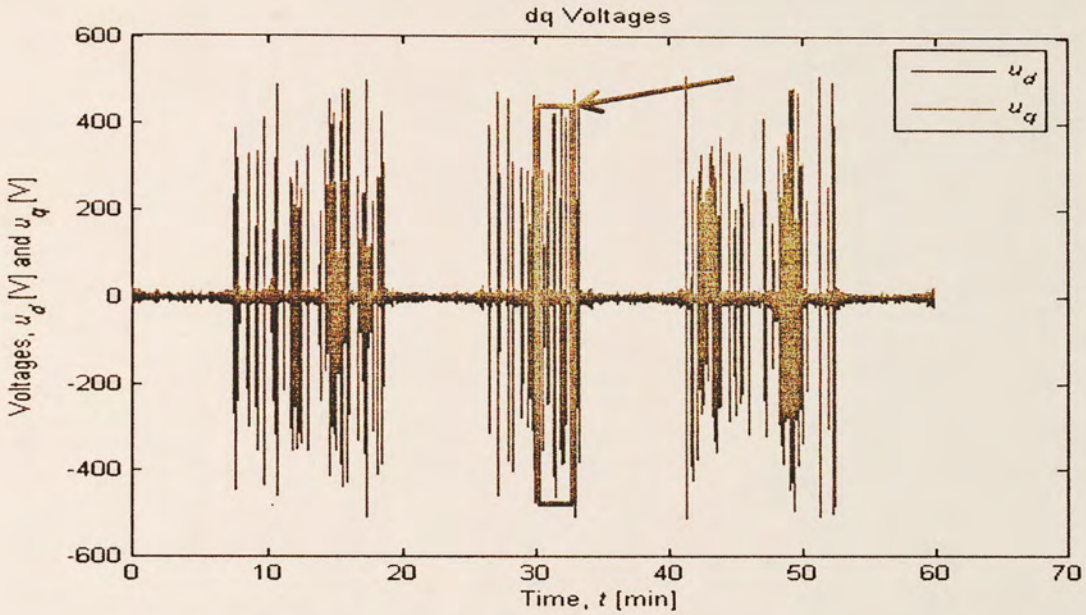

Figure 3-6 (a): Direct and Quadrature Voltages

The u_d voltage does not vary too much and generally stays around zero as seen in thE zoomed section of the graph.

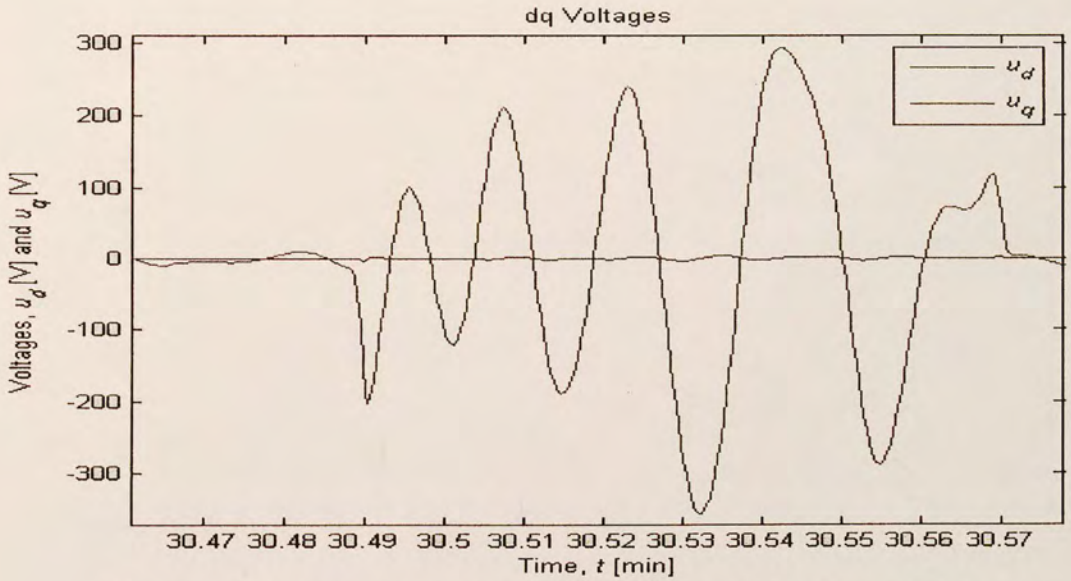

Figure 3-6 (b): Zoomed in Section of Direct and Quadrature Voltages

The copper winding inside the motor generate the most of heat. The transient heat generation is shown in Figure 3-7 with peak values near 2.5 Watts.

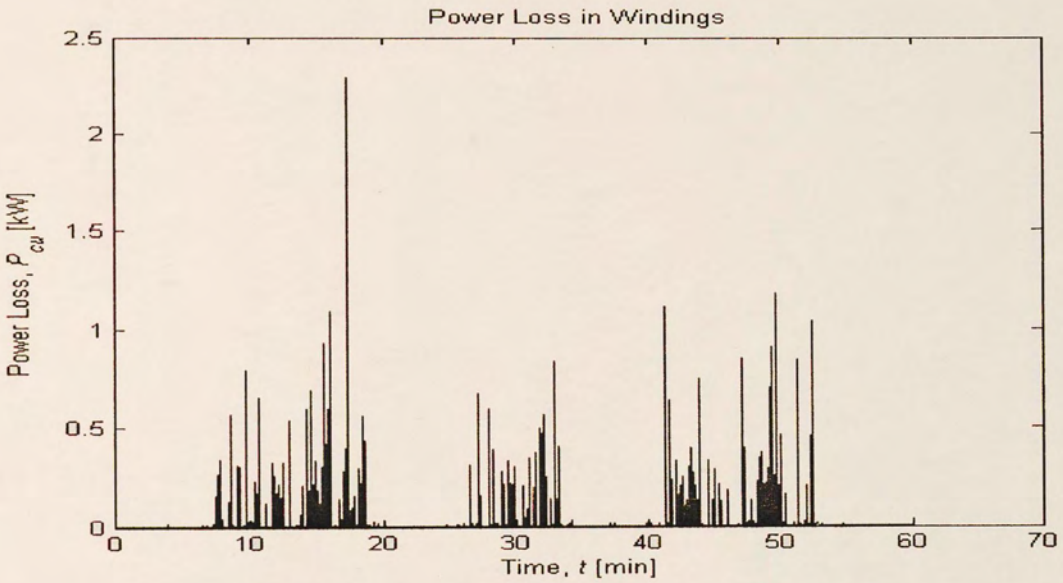

Figure 3-7: Copper Loss in the Motor Windings

Of great interest to power system engineers is the input power (positive values) and regenerative power (negative values) of the motor. The regenerative power represents power that is reintroduced to the system. Here we show the power in (blue) and power back into the EMA system (red) in Figure 3-8.

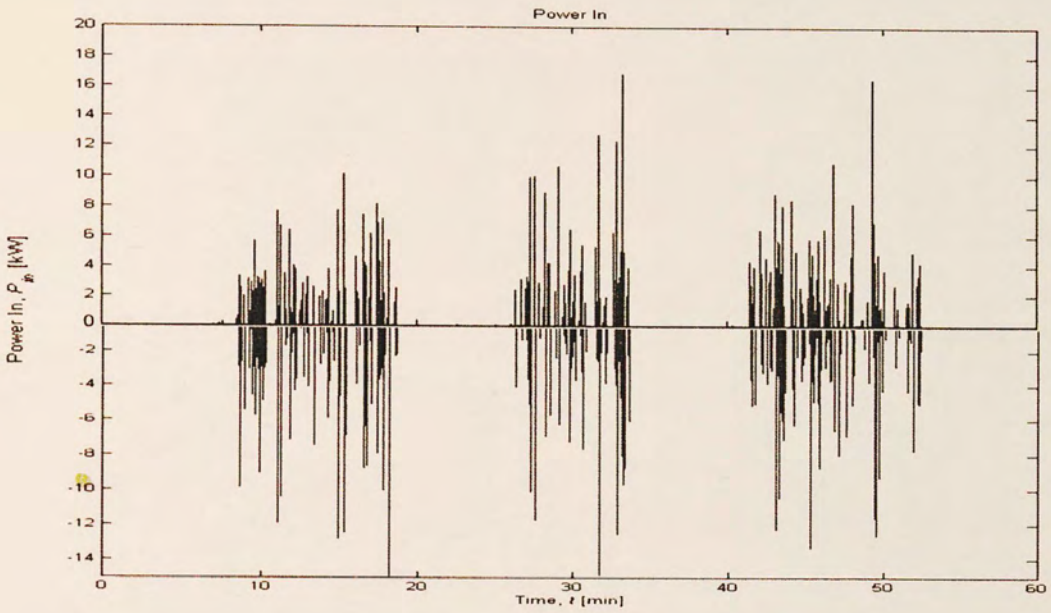

Figure 3-8: Power in and out

3.5 Conclusion

This chapter focused on a voltage control technique for PM motor design. The technique was based on voltage control. The fundamentals of this control scheme were based on the optimization of torque values by making the direct current and voltage as close to zero as possible. The profile was one hour flight profile indicating take off and landing. From the stroke profile the control indicated good stroke following,

Voltage and current values were reasonable leading to minimal power loss in the windings. Heat generation is another important aspect of the motor control. A study of integration algorithm speeds determined of the second order RK was indeed the fastest method for solving the dynamical equations. Models for heat generation in a motor during dynamic flight are necessary for design implementation. In Chapter 4 the experimentation of a different motor design will introduce a thermal profile lumped element model of the motor.

CHAPTER FOUR: EMA Testing

4.1 Introduction

At the Air Force Research Laboratories (AFRL) in Wright Patterson Air Force Base (WPAFB), EMA testing equipment is being set up. The EMA would run against a programmed, variable load (provided by a hydraulic press) while the temperatures and electrical behavior of the EMA are monitored. The plan then is to run the actuator through the stroke profile while the dynamic load on the actuator is provided by a hydraulic press.

The electrical and thermal behavior would then be measured and recorded through testing. The experimental setup, procedure, and results for the temperature reading during EMA operation will be the focus of this investigation. The MTS hydraulic press is the most critical piece of equipment. This press will produce the loads of a given mission profile. Currently the EMA motor under testing is only capable of 0.3 kW, future testing will involve 10 kW motors.

The hydraulic press is made by Instron and the controller is made by MTS. The press has a maximum stroke of 90 mm, a full-stroke frequency of 10 Hz, and a maximum force of 15,000 +/- 127.5 N. Its pump delivers 10 hp at 5 gal/min. The majority of all temperature, position, force, voltage, and current sensing and controlling the hydraulic press will be through the data acquisition system (DAQ). This National Instruments system will include an embedded controller with two partitions, one for loading Real Time OS (RTOS) and one for loading Windows XP. The RTOS will allow us to control

the hydraulic press with the most precision possible. The Windows partition will give us some additional programmatic ability. The DAQ will also be used to record all thermal, mechanical, and electrical data using two separate modules. One module will be a moderate-speed, high-channel count (32) board for thermal and mechanical sensing and another module will be a high-speed (3 MHz), low-channel count (8) board for electrical sensing. This will help reduce unnecessary data collection.

Considering the limitations of the EMA, the 10 hp motor simulated in this paper is not the actual motor tested in the experiment. The motor tested is a 10 pole 12 slot rated at 344W with a 120V AC source. This power rating is significantly lower than the rated power of the proposed design of 10 hp, however the testing procedure and methods will be the same once a new EMA is selected in the future to accommodate higher motor power ratings. All of the outputs of the control implemented for the test motor will not be shown and described. The thermal profile is the main focus of the section. The only output necessary to show and avoid duplication is the new stroke profile to indicate good stroke following and show the dynamics of the mission profile used for this thermal analysis

4.2 Thermal Modeling of Testing Motor

Some 3D models are provided below to visualize to the different components of the motor used in the lumped element model. An enclosed model of the motor is shown in Figure 4-1. This figure simply shows the outer casing of the motor, front opening, the rotor shaft and the front bearing.

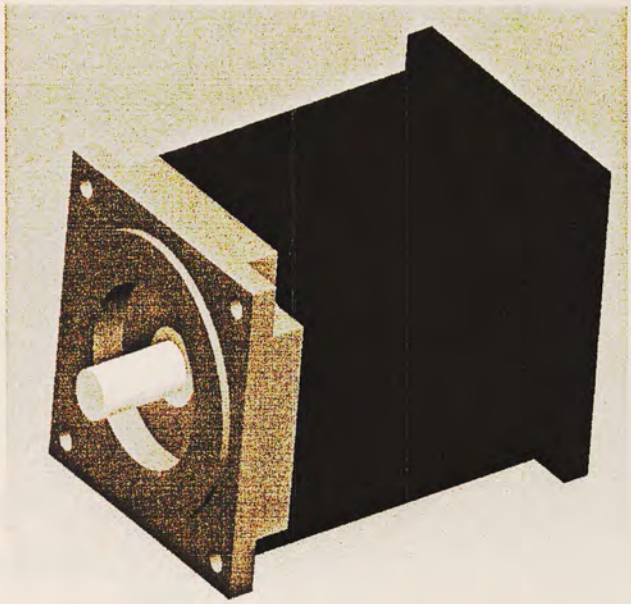

Figure 4-1: 3D Model of the PM Motor for Testing

Figure 4-2 shows the empty case with the stator pulled out. The motor contains different materials thus the need for different nodes. For example the outer aluminum case is considered one node and the permanent magnets of the rotor are another node.

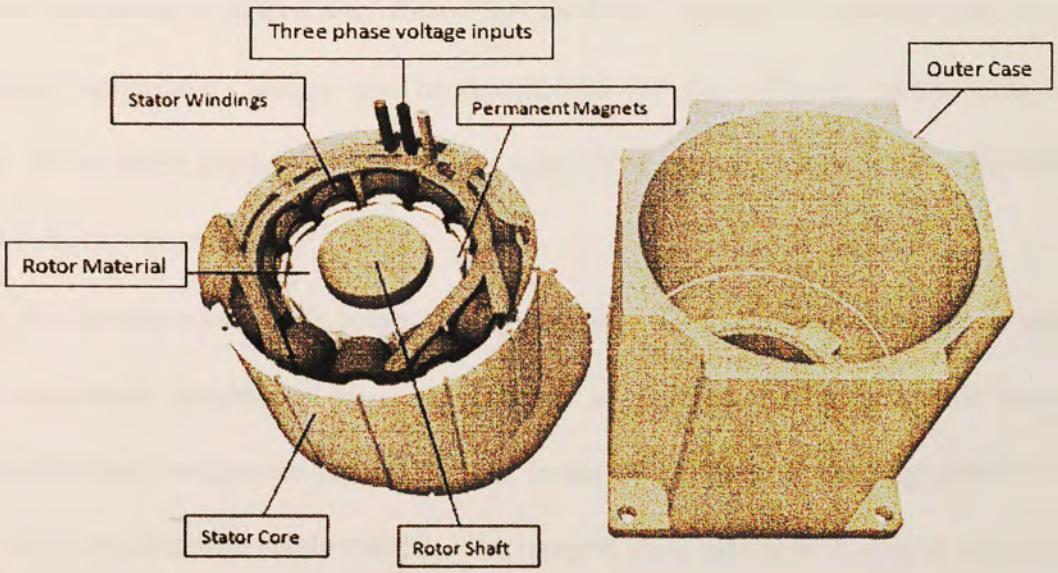

Figure 4-2: 3D Model of PM Motor (left) Stator and Rotor (right) Motor Casing

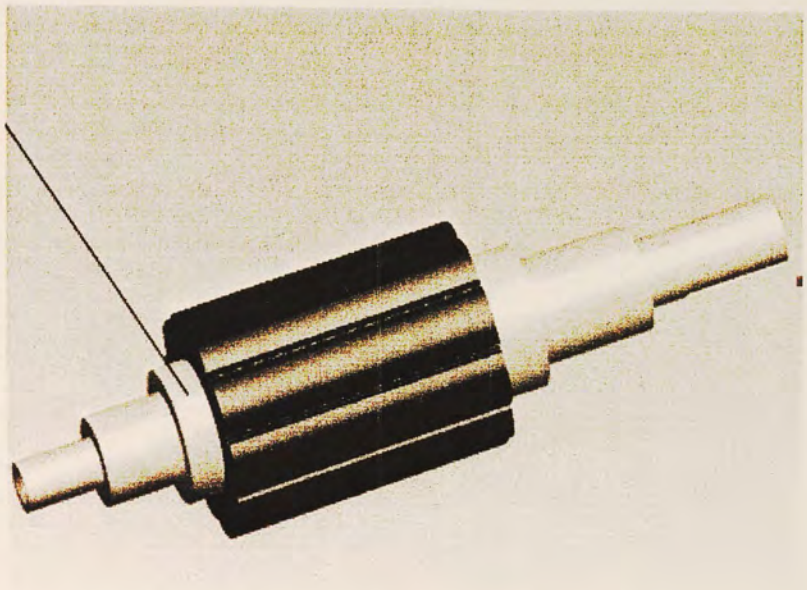

Figure 4-3: 3D Model of Rotor Structure

Typically to model the heat generation in a complete 3D model finite element analysis (FEA) is performed to get very accurate thermal readings. As described earlier the computational time of FEA is significant. Initially FEA can be used determine dynamic temperature ranges over the entire calculated domain. From this maximum and minimum temperature ranges can be determined for the different components of the motor. If the entire control model was run with FEM analysis inside it the computational time would be tremendous.

In this respect a single temperature, generally the average temperature, is used for each component determined by FEA. This is considered the lumped node approach. This much more computational feasible in terms of integration with the control of the motor and provides reasonable results. The lumped node model will now be addressed.

To properly represent all of the component average temperatures a node network is constructed. This network is represented by thermal resistance and capacitance values. The complete description of the this network will not be described but gives insight to what nodes are tested in the simulation and what is practical to test in the experiment. In practice, only a few locations or components are needed to assess the thermal behavior of the motor. It is not even feasible to test all these nodes in real reality.

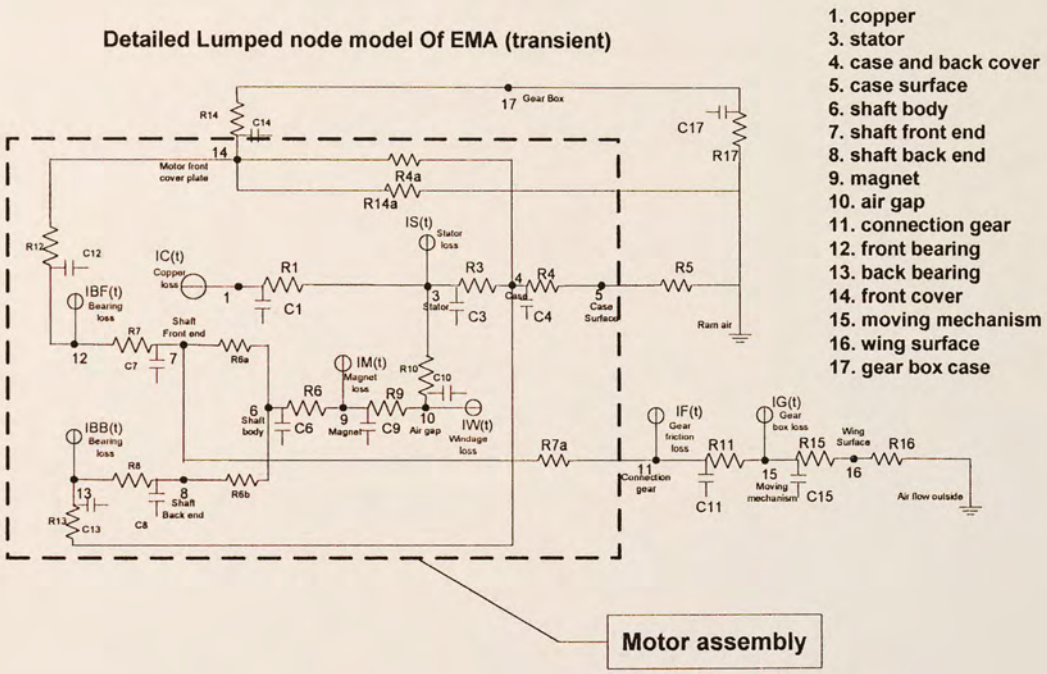

Figure 4-4: Lumped Element Model of EMA (Transient)

From this network capacitance values can be solved for using circuit analysis and solving for first order differential equations of R and C. Once these values are found the temperature response is properly modeled with varying losses in the motor as well as boundary conditions. When comparing FEA results for a few pertinent nodes in the motor it is seen that the lumped element model is a suitable substitute for the

computational intensive FEA calculations. Some of these nodes are also indicated in the cross-sectional view of the motor.

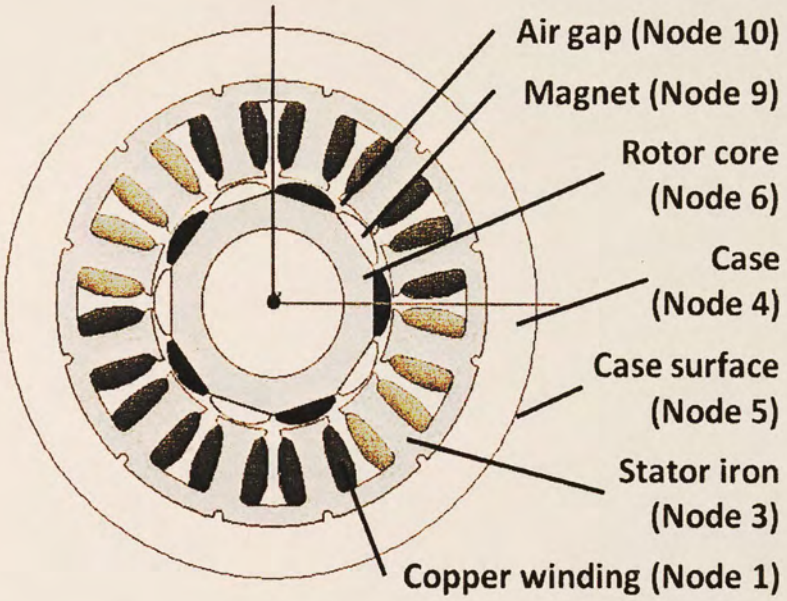

Figure 4-5: Thermal Node Locations on Motor

The lumped element mode shown in figure gives an idea to what nodes in the motor that need to be tested. The highest area of temperature is in the copper windings so finding the proper method to measure this temperature is critical to thermal analysis and verification. In the lumped element model there are a total of 13 nodes, however, all of these nodes cannot be tested and some really are not necessary to test. The experiment will be the method and procedure of placing thermocouples in as many critical thermal nodes in the motor as deemed necessary, and subsequently running a flight profile in the control of the EMA. The actual thermal effects can thus be analyzed. The thermal model results from the simulation are seen below.

Figure 4-4 represents all the nodes in the lumped element network. For the stroke and input torque profiles in Figure 4-5, Figure 4-6 shows temperature distributions of the nodes [24]. The diagram shows a starting temperature at ambient temperature 22°C and saturates around 25°C. With a temperature difference of 3°C and a spatial max ΔT of approximately 1°C the temperature readings are reasonable for motor operation of this flight profile.

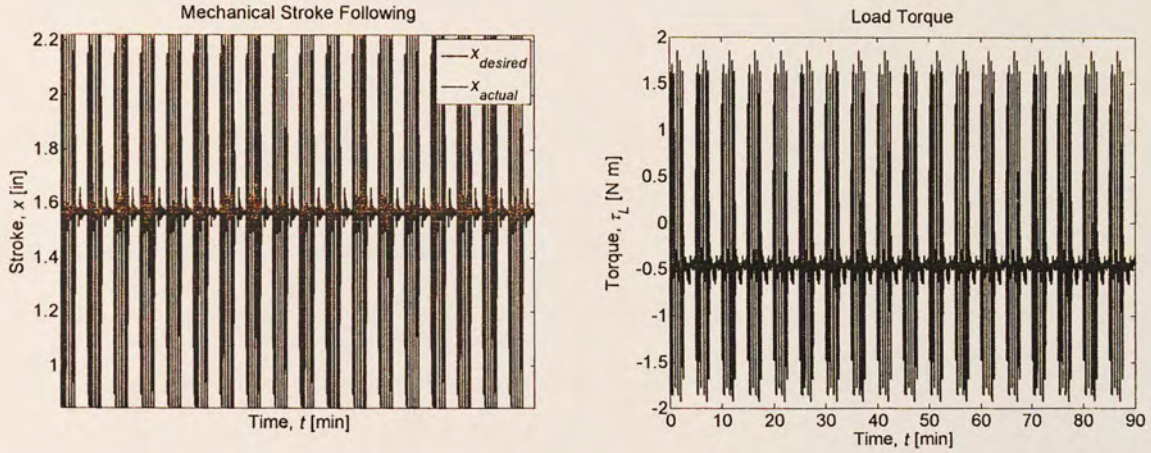

Figure 4-6: (left) Stroke and (right) Input Torque Profiles for Testing Motor

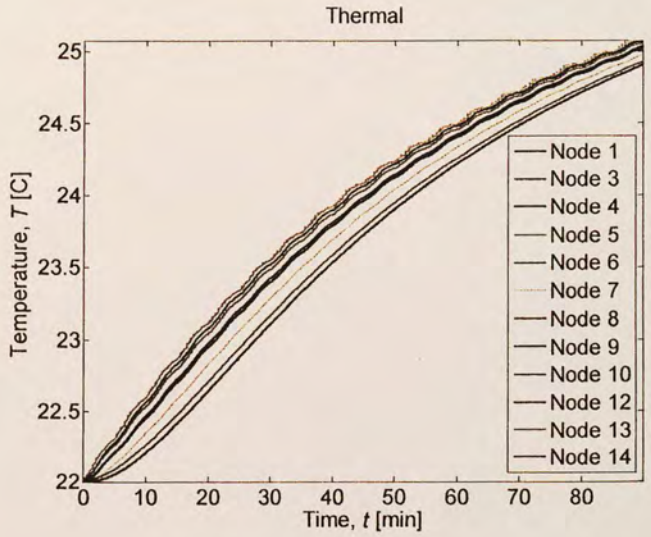

Figure 4-7: Temperature Distribution of Each Node in Testing Motor [20]

4.3 Experimental Setup

In order to validate the thermal simulation of the motor control simulation a proper experimental setup is the first step to this task. Currently there are two methods to in which will verify the software simulation results. The first method would be to load the force/stroke flight profile data directly into the simulation control as has been done in the beginning of this paper while simultaneously loading the same force data into the press and the same force data into the EMA. This method is depicted by the following flow diagram.

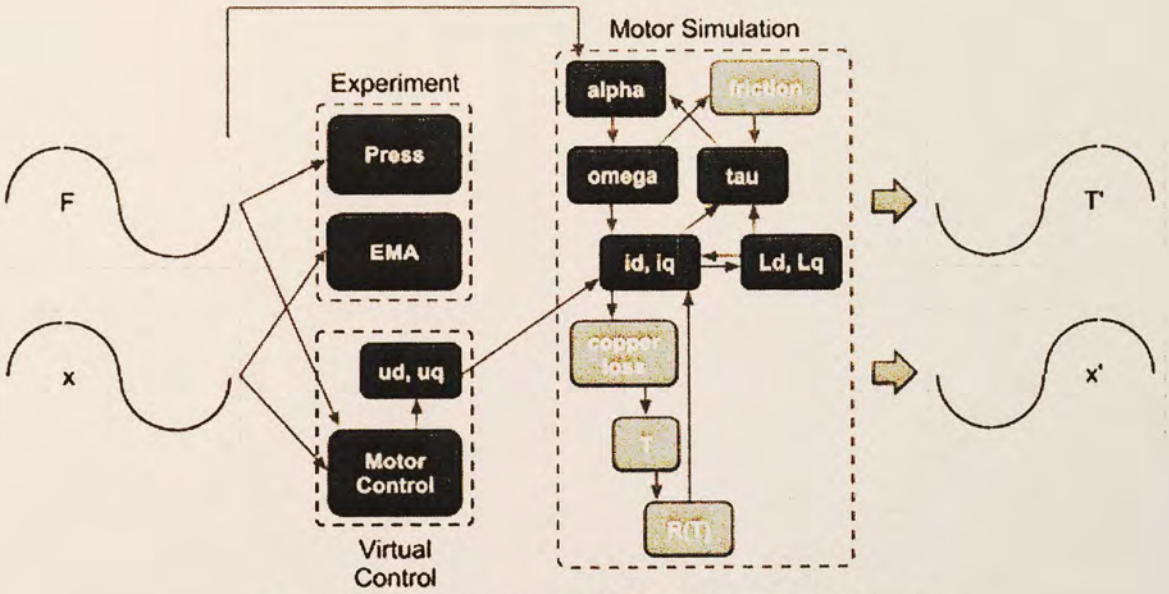

Figure 4-8: Experimental Flow Diagram Method I

As seen by this diagram the voltages used for the simulated control come from the voltages calculated by the software. Running the experiment and simulation simultaneously is the goal of this experiment allowing the user to compare accuracy of simulation in real-time. The second method and the method in which we will actually use is depicted by the next figure.

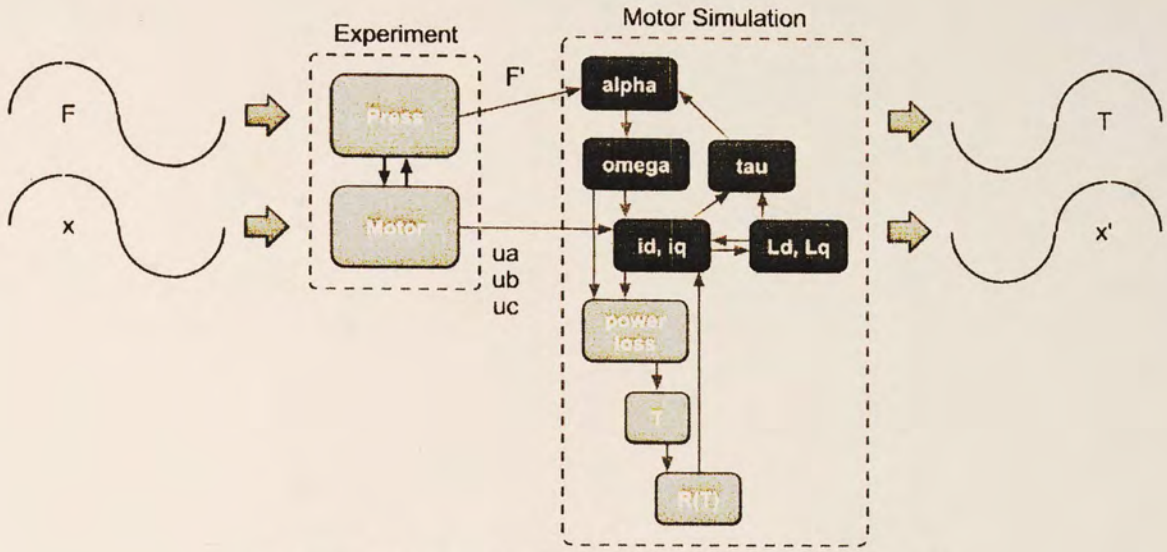

Figure 4-9: Experimental Flow Diagram Method II

In this method force profile data will be input in the press while stroke profile data will be input into the motor. The actual voltages of the motor, note the simulated voltages will be used for the simulation. This method seems to be the most precise method of validation of the software model. It ensures that the same input voltages of the motor will be the same input voltages of the simulation.

All of the hardware components for experimentation and their function will be described. Preparation to the experiment will include all necessary procedures for operation and setup of the equipment. The experiment will use thermal couples embedded into the motor at the nodes deemed critical for software validation. The placement and setup for placement of the thermocouples will also be described here.

Hardware	Description
MTS Hydraulic Press	Framework that houses the actuator and motor as well as the hydraulic press that provides load force for the actuator. (See figure 10)
NI Data Acquisition System	This National Instruments system will include an embedded controller with two partitions, one for loading Real Time OS (RTOS) and one for loading Windows XP. The RTOS will allow us to control the hydraulic press with the most precision possible. The Windows partition will give us some additional programmatic ability. The DAQ will also be used to record all thermal, mechanical, and electrical data using two separate modules. One module will be a moderate-speed, high-channel count (32) board for thermal and mechanical sensing and another module will be a high-speed (3 MHz), low-channel count (8) board for electrical sensing. This will help reduce unnecessary data collection. (See Figure 11)
EMA with Motor	The Danaher EMA is a linear actuator that is currently capable of 3kW from the motor. The maximum stroke length is 12 inches however for our experiment only 4 inches are used. (See Figure 12)
BNC Breakout Panel	This panel contains 16 BNC input connection and 2 BNC outputs used for voltage commands to the press as well as feedback from the load sensor in the EMA. (See figure 15)
MTS Press Controller	This controller is responsible for controlling the valve of the hydraulic press. (See figure 13)
Danaher Motor Controller	This controller is responsible for what voltages are sent to the motor that translate into speed. (See figure 13)
Power Supply	Simply provides power to the workstation. (See figure 14)
PC	Computer loaded with LabVIEW. (See figure 13)
Terminal Block	Allow inputs from the thermocouples for readings in LabVIEW. The terminal block contains 32 inputs. (See figure 16)

Table 4-1: Experimental Hardware Descriptions

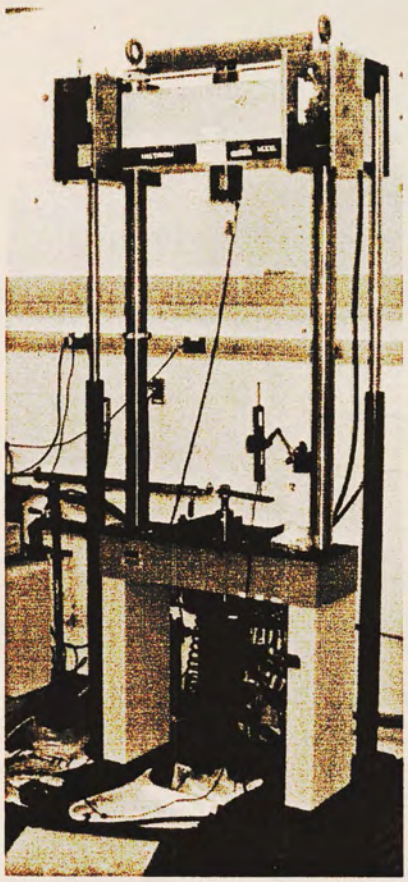

Figure 4-10: MTS Hydraulic Press

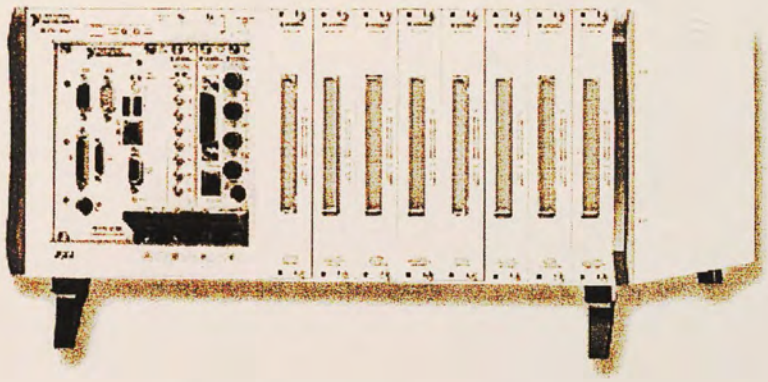

Figure 4-11: NI Data Acquisition System

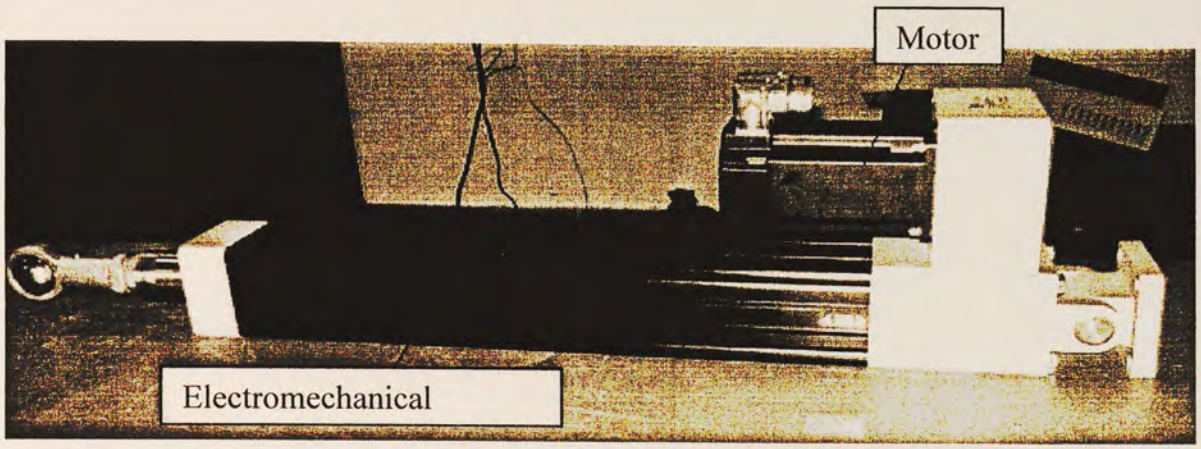

Figure 4-12: Danaher Motion EMA with Motor

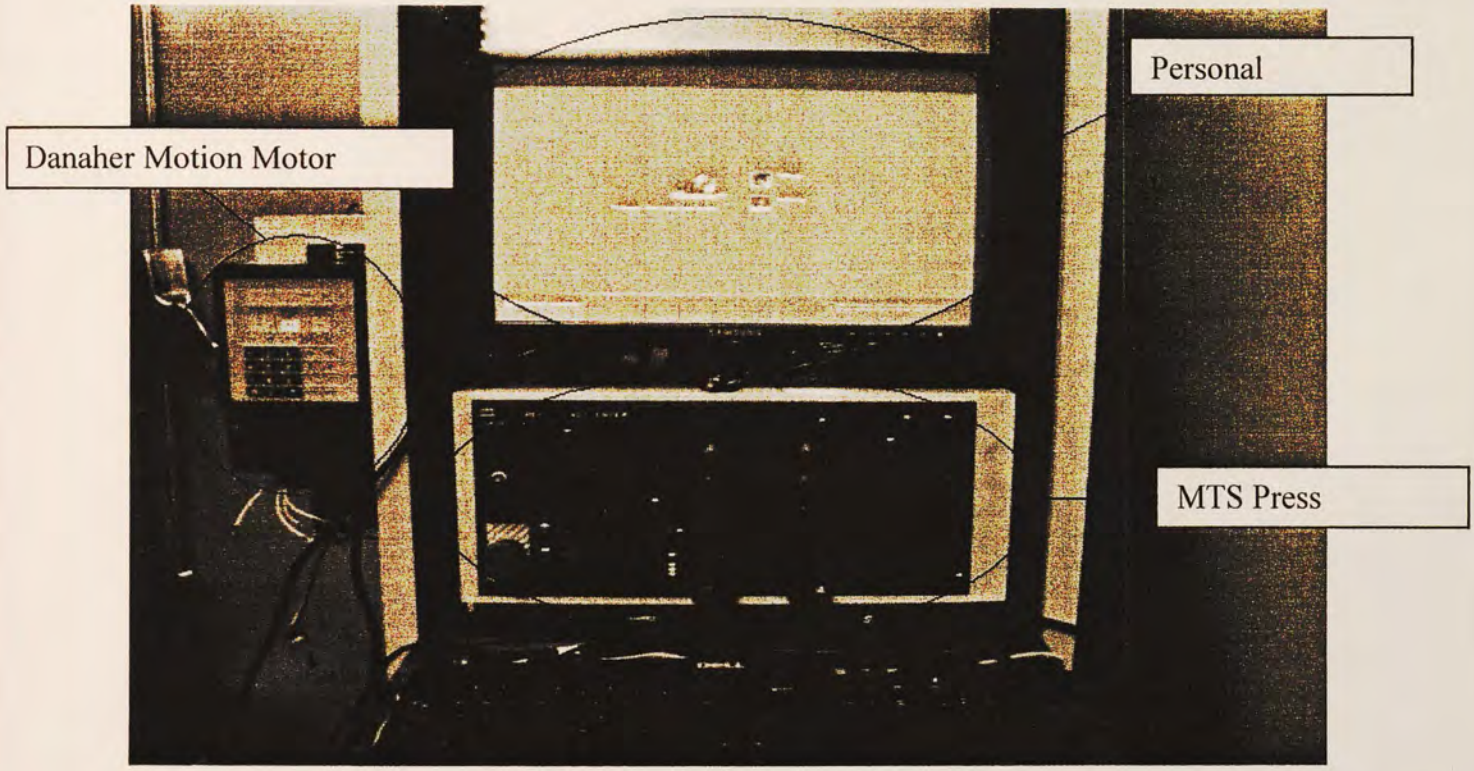

Figure 4-13: PC, Motor Controller, MTS Press Controller

Figure 4-14: Power Supply

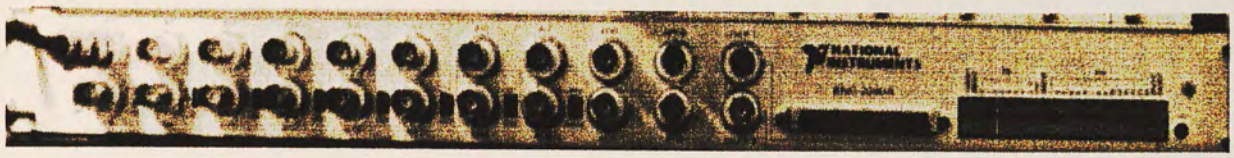

Figure 4-15: Breakout Box

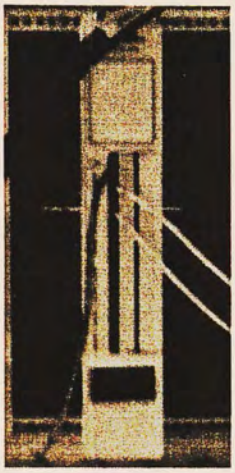

Figure 4-16: SCXI-1303 Terminal Block

In preparation to the experiment the determination of what areas (nodes) in the motor to be tested for temperature was determined. As depicted by the lumped element model in figure 7 there are a total of 13 nodes that were used. It is not practical or feasible for all of these nodes to be tested as some of the nodes are located on the rotor. Therefore it was determined that testing the copper windings, the stator core, and the aluminum case of the motor was more practical and can provide the most pertinent data. The locations of these probes are indicated in the following diagram.

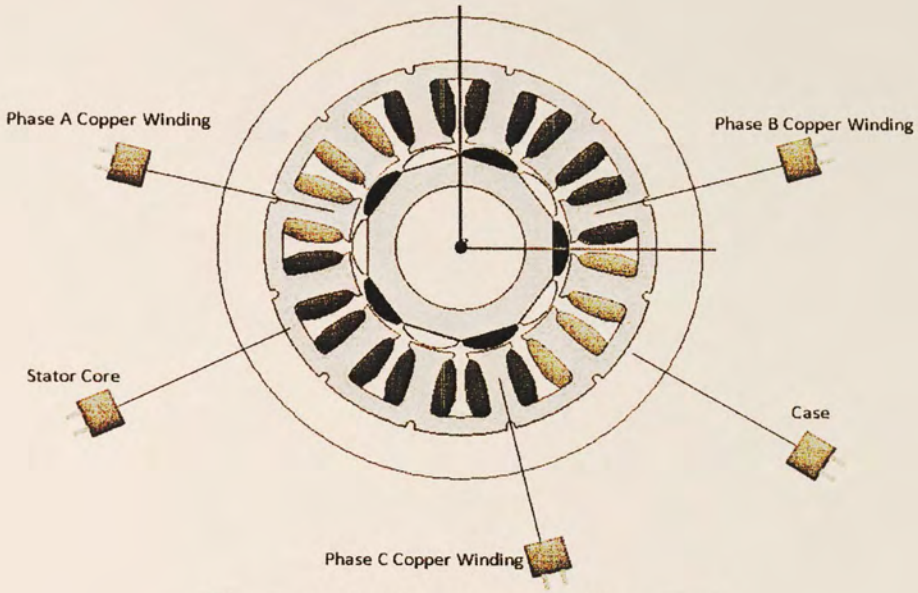

Figure 4-17: Thermocouple Placement

In order to place these thermocouples into the motor, small holes will be drilled. Notice that the thermocouples used to measure the heat of the copper windings are placed in the tooth of the stator. This is the closest we can get to the copper windings without building a motor from scratch and placing the thermocouples into the copper winding configuration. There is a copper winding thermocouple for each phase. The other two thermal couples will test the backwall of the stator core and the other will test heat generated in the aluminum case. The thermocouples are T-type quick disconnect probes. The female connection has wire that connects to the terminal box on the NI DAQ.

Step	Description	Notes
1	PC power and setup	Ensure that the host PC (known as the "MTS") is turned on. The login password is MTS. Once logged in open up the national instruments software program LabVIEW. Inside of LabVIEW open the file named '9_ja_PIDF.VI.
2	Press controller power and setup	Verify that the MTS controller is on. The controller is named "MTS 458". This device is usually kept on so simply verify if the display contains a load value or there are LEDs light up.
3	Pump Power	The hydraulic pump must be turned on. There is a switch on the pump to turn it on. If the pump does not turn on ensure the breaker has not been popped and the both of the red emergency stop buttons are not engaged.
4	EMA installation	The EMA is placed in the press with the motor at the top. If the ball and socket joint of the EMA do not align properly with the clevis joint of the "jogging" command must used in LabVIEW to help alignment.
5	Thermal couple insertion	There will be a total of 10 thermo couples that are inserted into the motor for temperature readings. Insert T type rigid thermo couple probes into all the designate areas as indicated by figure. These will be the nodes that are tested during the experiment.
6	Cable connections	There are two cables which must be attached to the BNC breakout panel on the front of the cabinet. The cables are always attached to the left side of the cabinet where they are also labeled. The cable labeled 'external in' should be connected to "A01" (analog output 1). This is the cable that will transmit the voltage commands from the LabVIEW VI to the press (load control). The cable labeled 'feedback in' should be connected to "AI1" (analog input 1). This cable will provide the load sensor feedback data to the LabVIEW controller from the real press activity.
	Terminal block connection	All of the thermocouples must be connected by wire to the SCXI-1303 terminal block. The terminal block has 32 analog inputs. Connect the wire from the thermocouples to anyone of the inputs but keep track of what terminal pertains to what node in the motor.

Table 4-2: Experimental Setup

4.4 Testing Procedure

Now that hardware and software setup is complete performing the actual test is the next step. The testing will be initiated by synchronization of the EMA and the press. The LabVIEW script contains the code for the press control and synchronization. The control scheme of the simulation will be embedded in this script in order to obtain the voltages created by the motor through the flight profile data.

Step	Description	Notes
1	LabVIEW code operation	Open national instruments LabVIEW '9_jan_PIDF.VI'. The LabVIEW code maintains press control as well as synchronization between the press and EMA. This should be started before the EMA is started. This script will log the temperature data as well as voltage per cycle. The MATLAB simulated controller has been embedded in this LabVIEW script to allow the actual input voltages of the motor to enter the simulated control
2	EMA operation	The EMA connects to the EMA driver with two cables. The EMA driver, which handles power and control electronics is turned on by plugging it in.
3	Load motion profile	The load the mission profile used should be saved in a text document and save to the desktop of the PC. In order to run profile select click the run button and the dialog box will allow the user to browse for the text file. Find the text file and click ok.
4	Run Experiment	The program will run automatically after selecting ok in the dialog box.
5	Stop Experiment	The end of the experiment is indicated by the length of the motion profile data. Once there is no more motion data the experiment has ended.

Table 4-3: Experimental Testing Procedure

In LabVIEW the waveform generator function will indicate the voltage and current values produced by the motion profiles. The thermocouple data will also be shown. This data will be collected over a time period specified by the user. Different windows will display voltage and current for both of the experiment and simulation as well as windows to regulate each thermocouple.

If the same profile that was used for the simulated control for this motor simulation, the experiment should show an increase of temperature from ambient air at 22°C to approx. 57°C over a two hour simulation. There can be various profile input in the press and EMA. Therefore, with various profiles expected results have not been determined. The important notion is the same voltages for the experiment and the simulated control are used simultaneously. This indicates that the temperature profiles should be close to the same with minimal error.

4.5 Expected Results, Sensitivity, and Uncertainty

The thermal results of this simulation are ultimately the basis for comparison. Note that analyzing the thermal results is based on the mission profile. Thermal simulation results for the second stroke profile indicate approximately a 5 degree shift from 22°C to 27°C. Due to the fact that we are taking the voltages from the actual motor and input them into the control reduces some of the error of comparing the calculated control voltages and the actual voltages. Despite this reduction in error there are still different aspects of the experiment that must be considered in order to ensure that experimental results are within a reasonable range of the simulation results.

In simulation the calculations and results take on a more ideal scenario. In real world experimentation there are more devices, losses and uncertainties to be considered. Sensitivity of instrumentation is also a factor in experimentation. Sensitivity analysis for example is required when measuring temperature on a particular surface. A surface will generally contain a temperature gradient where the readings may be different based on the location of the measurement. In the simulation, however, a lumped element approach is implemented and no temperature gradient for each node of the network is depicted. Each lumped element is considered to maintain the same temperature values.

This leaves the uncertainty of the components that are measuring temperature, voltage and current. These uncertainties must be accounted for and calculated to allow a specific error range for the measured values. The uncertainty will be calculated by first understanding which components must be accounted for in the experiment. Once this is done calculations based on all the involved components will be performed to allow a sort of error band to the range of values measured. For example, if a thermocouple measuring the winding heat generated falls within a certain range of values then it is considered valid. In order to validate the simulation the temperatures derive in the simulation would have to also fall within the same range of values.

The components involved in the experiment with their respective uncertainties.

Component	Range	Uncertainty
Postion Sensor	± 50 mm	± 1% of Range
Load Sensor	± 15 kN	± 1% of Applied Force
DAQ card for voltage and current sensing (PXI-6255)	± 10 V	± 1950 μV
Thermalcouple Input Module (SCXI-1102)	± 10V	± 100 mV
Thermalcouple Terminal Block (SCXI-1303)	15°C to 35°C 0°C to 15°C and 35°C to 55°C	± 0.5°C ± 0.85°C
Thermalcouple	220°C	± 0.1 °C

Table 4-4: Uncertainty Analysis

From these considerations of uncertainty, ranges of values can be examined an analyzed to determine whether the values measured are indeed reasonable

4.6 Conclusion

The topics discussed in this section include the analysis results of a flight profile data looped multiple times, experimentation technique, testing procedure, and comments on expected results which incorporates uncertainty analysis. The experiment used a different motor design as the one proposed in the paper. The purpose of the experiment

is to validate the simulation package so the results must be compared. Even though this alternative design was used, validation of the software will open the doors for implementation of different motor designs including motor designs similar to the proposed motor design.

CHAPTER FIVE: CONCLUSIONS

From this research a few broad areas of study were emphasized. The background and scope for the implementation of the EMA in aircraft laid the foundation of demand for high performance electric motor design. Therefore, a complete design methodology was described for the surface mounted PM motor. The design methodology was developed for the case of a multi-pole rotor which translates into alternative derivations for airgap length. Proper sizing of the 10krpm, 10hp motor are solved for through the PM designer.

These sizing values as well as other design specifications are input into a software program called RMXprt for analysis. From this software a design efficiency of 95% was achieved at 10krpm. Once this design was validated the implementation of a control of this motor was the next area of interest. A linear voltage control scheme proved to show excellent stroke following. The analysis of a 1 hour mission profile showed output values of dq current and voltage, as well as input power, regenerative power, and power loss in the windings of the motor.

When solving for the dynamical equations that govern the characteristics of the motor, different algorithms were used for comparison. It was shown that the 2^{nd} order RK method was the fastest with sufficient accuracy. The last area of interest was development of an EMA testing procedure on an alternative motor design then described in chapters two and three. The design consisted of a 10 pole 12 slots. The simulation used to compare to the experiment included a thermal lumped element model. The purpose of this experimental procedure is to validate the software for future motor design

configurations. An uncertainty analysis was necessary for the different testing equipment.

EMA technology implementation for all electric aircraft is a feasible goal. With the combined efforts on development of more efficient motor design, thermal management of the motor and the controller, as well as prognostics and health management, EMA technology will surely be used in 6^{th} generation military aircraft. The impact of the technology can reach multiple facets of industry making further research more attractive. Potential in this field of study has much to offer the needs of the future, and the reality of this is only a matter of time.

LIST OF REFERENCES

[1] Spitzer, C. R., Hood, R. V., "The All Electric Airplane - Benefits and Challenges", *Proceedings of the Aerospace Congress and Exposition, Anaheim, CA; United States; 25-28 Oct. 1982,* SAE 821434, Society of Automotive Engineers (SAE), Warrendale, PA, USA, 1982.

[2] Moir, I., "The All-Electric Aircraft - Major Challenges", *Proceedings of the IEE Colloquium on All-Electric Aircraft,* Ref. no. 1998/260, The Institution of Electrical Engineers (IEE), Savoy Place, London, UK, 17 June 1998.

[3] Bataille, N., *Electrically Powered Control Surface Actuation*, MS thesis, Cranfield University, Bedfordshire, UK, 2006.

[4] Pointon, J. M., *Thermal Management of Electromechanical Actuation on an All-Electric Aircraft*, MS thesis, Cranfield University, Bedfordshire, UK, 2007.

[5] Woodburn, D. A., Wu, T. X., Chow, L., Leland, Q., Brokaw, W., Bindl, J., Rolinski, N., Zhou, R., Lin, Y., Jordan, B., "Dynamic Heat Generation Modeling of High Performance Electromechanical Actuator," *48th AIAA Aerospace Sciences Meeting Including the New Horizons Forum and Aerospace Exposition*, Paper No. AIAA-2010-290, Orlando, Florida, Jan. 4-7, 2010.

[6] Ku, J., Ottenstein, L., Kaya, T., Rogers, P., Hoff, C., "Testings of a Loop Heat Pipe Subjected to Variable Accelerating Forces, Part 1: Start-up," *International Conference on Environmental Systems*, July 2000, Toulouse, France, SAE 2000-01-2488, 2000.

[7] Vrable, D. L. and Yerkes, K. L., "A Thermal Management Concept for More Electric Aircraft Power System Applications," *Aerospace Power Systems Conference,* SAE 981289, Williamsburg, VA, April 1998.

[8] Gievas, J. F., Wing, M., *Permanent Magnet Motor Technology,* Marcel Dekker, Inc., 2002.

[9] Cheng, M., Chau, K. T., Chan, C. C. "Static Characteristics of a New Doubly Salient Permanent Magnet Motor," *IEEE Transactions on Energy Conversion,* vol. 16, pp. 20-25, Mar. 2001.

[10] Mino, M., Tanaka, T., Homma, M., "Difference between Temperature Dependences of both Initial Permeability and Maximum Permeability of Sendust Alloys," *IEEE Transactions on Magnetics,* Vol. 21, pp. 1240-1244, May 1985.

[11] Fitzgerald, A. H., Kingsley, C. J., Umans, S. D., *Electric Machinery*, 6th ed., NY: McGraw-Hill, 2003.

[12] Huang, S., Luo, J., Leonardi, F., Lipo, T. A., "A General Approach to Sizing and Power Density Equations for Comparison of Electrical Machines," *IEEE Transactions on Industry Applications,* Vol. 34, pp. 92-97, 1998.

[13] Constantinides, S. "Understanding and Using Reversible Temperature Coefficients," http://www.arnoldmagnetics.com/, 2009.

[14] Constantinides, S., "Magnet Selection," http://www.arnoldmagnetics.com/, 2003.

[15] Schobinger, D., Gutfleisch, O., Hinz, D., Müller, K., Schultz, L., Martinek, G., "High Temperature Magnetic Properties of 2:17 Sm–Co Magnets," *Journal of Magnetism and Magnetic Materials*, Elsevier, Vol. 242-245, pp. 1347-1349, 2002.

[16] Stone, G. C., Boulter, E. A., Culbert, I., Dhirani, H., *Electrical Insulation for Rotating Machines,* IEEE Press Series on Power Engineering, John Wiley and Sons, Inc., 2004.

[17] Huynh, C., Zheng, L., Acharya, D., "Losses in High Speed Permanent Magnet Machines in Microturbine Applications," *Journal of Engineering for Gas Turbines and Power,* vol. 131, paper No. 022301, March 2009.

[18] Wang, F., Xu, Y., Kong, X., Zhang, D., "Study of Core Loss on High Speed PM Machines," *IEEE International Conference on Industrial Technology (ICIT 2009),* p.1-4, Gippsland, VIC, 2009.

[19] Hanselman, D. C., *Brushless Permanent-Magnet Motor Design,* McGraw-Hill, 1994.

[20] Woodburn, D., Wu, T., Lin, S., Bindl, J., Hu, Y., Brokaw, W., Chow, L., Zhou, L., Lin, Y., LeLand, Q., Tran, B., Jorda,, B., Gregory, E., Iden, S., and Rolinski, N., "Integrated Nonlinear Dynamic Modeling and Field Oriented Control of Permanent Magnet (PM) Motor for High Performance EMA," to appear in *SAE Power System Conference,* Fort Worth, TX, Nov. 2010.

[21] Dolinar, D., Weerdt, R. De, Freeman, E. M., "Calculation of Two-axis Induction Motor Model Parameters Using Finite Elements," *IEEE Transactions on Energy Conversion*, Vol. 12, No. 2, pp. 133-142, 1997.

[22] Topcu, E. E., Kamis, Z., Yuksel, I., "Simplified Numerical Solution of Electromechanical Systems by Look-up Tables," *Mechatronics*, Vol. 18, No. 10, pp. 559-565, Elsevier, 2008.

[23] Lipo, Thomas A., Consoli, Alfio, "Modeling and Simulation of Induction Motors with Saturable Leakage Reactances," *IEEE Transactions on Industry Applications*, Vol. 20, No. 1, pp. 180-189, 1984.

[24] Ong, Chee-Mun, *Dynamic Simulation of Electric Machinery*, Prentice Hall, 1998.